

POSITION CONTROL  
COMPARISON OF EQUILIBRATED  
AND MASS COUNTERWEIGHT  
SYSTEMS

Angela Carr

A thesis submitted in partial fulfillment of  
the requirements for the degree of

Masters of Science

in

Mechanical Engineering

Dr. Charles Reinholtz, Chair

Dr. Don Leo

Dr. William R. Saunders

March 30, 2001

Virginia Polytechnic Institute and State  
University

Keywords: Equilibrator, Control, Dynamic Model

Virginia Polytechnic Institute and State  
University

Abstract

POSITION CONTROL  
COMPARISON OF  
EQUILIBRATED AND MASS  
COUNTERWEIGHT SYSTEMS

by Angela Carr

In robotic systems, reduction of inertia is a key concern. One way to reduce the system inertia is to replace counterbalance masses with an equilibrator, which is a force element like a spring. Although there has been much research on equilibrated mechanisms, there has not much research on the control of these mechanisms. This thesis explores the PID control of equilibrated systems, and compares the results to the PID control of a common method of equilibration, the mass counterweight. Through modeling, simulating, and testing of the two systems, the equilibrated system response was found to be superior to the mass counterweight in measures of settling time and peak overshoot.

## TABLE OF CONTENTS

1.0	Introduction.....	1
1.1	Definition of Equilibration .....	2
1.2	Literature Review .....	3
1.3	Project Scope.....	10
2.0	System Modeling.....	11
2.1	Modeling the Motor.....	12
2.1.1	Electrical and Mechanical Motor Model .....	12
2.1.2	Experimentally Finding Motor Model Parameters .....	14
2.1.3	Equivalent motor model with a gear reducer.....	19
2.2	Modeling the Mass Counterweight system .....	19
2.3	Modeling the Equilibrated System .....	21
2.4	State Space Model .....	26
3.0	System Simulations.....	28
3.1	Mass Counterweight.....	28
3.1.1	System Properties .....	28
3.1.2	Nonlinear and Linear Dynamic Simulations .....	30
3.2	Equilibrated System.....	30
3.2.1	Geometric Relationship .....	31
3.2.2	Homogeneous Simulation .....	32
3.2.3	System Properties .....	33
3.2.4	Nonlinear and Linear Dynamic Simulation.....	35
3.3	Controller Simulations.....	36
3.3.1	PID and Digitization Review.....	37
3.3.2	Mass Counterweight System Controller.....	38
3.3.3	Comparison of Simulated Systems.....	39

<b>4.0</b>	<b>System Experiment</b> .....	<b>41</b>
4.1	Mechanical Hardware Setup.....	41
4.2	Data Collection.....	42
4.3	Electrical System.....	45
4.3.1	Encoder.....	45
4.3.2	Amplifier and Battery.....	47
<b>5.0</b>	<b>Results and Conclusions</b> .....	<b>51</b>
5.1	Experimental Results.....	51
5.2	Experimental Results Using Optimized PID Controller.....	52
5.3	Comparison of Experimental and Simulated Results.....	54
5.4	Conclusions.....	57
	<b>Bibliography</b> .....	<b>58</b>
	<b>Vita</b> .....	<b>64</b>

## LIST OF FIGURES

<i>Number</i>	<i>Page</i>
Figure 1: Picture of vehicle carrying a counterbalanced arm.....	2
Figure 2: Basic Equilibrator Model.....	4
Figure 3: Self-Adjusting Equilibration Mechanisms [Nathan, 6].....	5
Figure 4: Tension and Compression Spring Equilibrated Record Player Arm .....	5
Figure 5: Model Used to Derive Quasi-Exact Spring Equilibration .....	6
Figure 6: Vertical design example, pantograph [Streit and Shin, 13] .....	7
Figure 7: Parallel design example [Streit and Shin, 13].....	8
Figure 8: Prismatic equilibration example [Streit and Shin, 13].....	9
Figure 9: Countermass System.....	11
Figure 10: Equilibrated System.....	11
Figure 11: Breakdown of Motor and Encoder.....	12
Figure 12: Free body diagram of the mechanical component of the DC motor .....	13
Figure 13: Circuit diagram of the electrical components of the DC motor .....	13
Figure 14: Experiment to Determine $k_b$ , Back-emf .....	14
Figure 15: Experimental Setup.....	15
Figure 16: Model of Experimental Setup.....	15
Figure 17: Actual and Estimated Frequency Responses Functions.....	18
Figure 18: Model of Motor with Gearbox.....	19
Figure 19: Mass Counterweight Model.....	20
Figure 20: Equilibrator model .....	21
Figure 21: Dimensioned Equilibrator model .....	22
Figure 22: Enlarged Equilibrator Model Showing Four-Link Position Loop .....	23
Figure 23: Equilibrator Maximum Position.....	25
Figure 24: Pole Map of Mass Counterweight System.....	29
Figure 25: Open Loop Bode Response of Mass Counterweight System.....	29
Figure 26: Linear and Nonlinear Dynamic Simulation .....	30
Figure 27: Relationship between $\theta$ and Cable Length.....	31
Figure 28: Relationship between $\theta$ and $\Delta x$ .....	31
Figure 29: Relationship between $\phi$ and $\theta$ .....	32

Figure 30: Pole Map of the Equilibrated System .....	34
Figure 31: Open Loop Bode Plot of Equilibrated System.....	34
Figure 32: Dynamic Equilibrator Response with IC of Theta=0.....	35
Figure 33: Dynamic Equilibrator Response with IC of Theta=45.....	36
Figure 34: Simulation of Controlled Mass Counterweight system .....	38
Figure 35: Closed Loop Position Response of Mass Counterweight System to a Step Input .....	39
Figure 36: Control Voltage of Mass Counterweight System Equilibrated System Controller.....	39
Figure 37: Closed Loop Position Response of Equilibrated System.....	39
Figure 38: Control Voltage of Equilibrated System.....	39
Figure 39: Simulink Block Diagram Showing Closed-Loop Control of Systems.....	43
Figure 40: ControlDesk <sup>®</sup> Layout.....	44
Figure 41: Electrical System .....	45
Figure 42: dSPACE <sup>®</sup> controller board Setup for Experiment .....	46
Figure 43: Voltage Divider Circuit Specified in dSPACE <sup>®</sup> Manual.....	47
Figure 44: Inside the Copley Control Corp. Amp .....	49
Figure 45: Experimental Position Response using Comparator Controller.....	51
Figure 46: Experimental Results of Mass Counterweight System using an Optimized PID Controller .....	52
Figure 47: Experimental Results of Equilibrated System using an Optimized PID Controller .....	53
Figure 48: Closed Loop Position Response of Mass Counterweight System to a Step Input .....	54
Figure 49: Control Voltage Comparison of Mass Counterweight System.....	55
Figure 50: Closed Loop Position Response of Equilibrated System to a Step Input .....	56
Figure 51: Control Voltage Comparison of Equilibrated System .....	57

## ACKNOWLEDGMENTS

There are many people who would have supported me at Virginia Tech. But, my time at school would not be nearly as rich without the support and friendship of Dr. Charles Reinholtz. He has been an advisor, teacher, counselor, and friend throughout the years. I do not know what I would have done without his levity, realistic approach, and his ability to listen and care. Thank you from the bottom of my heart.

I would also like to thank my friends and family for their support. They always put up with the many hours of office work, and the constant explanation, "I have to work." They provided the outlets; eating taco salads, river escapades, parties, working out, and trips to Cheasepeake, Florida and Georgia; which I needed to maintain an even keel. They provided a sounding board for my technical questions and answers. In many ways, they should be co-authors of this work. A special thanks to Kevin who understands my thesis as well as I do, and for spending hours on "sanity checks." Also, thanks to Mom Riess who has been my friend and advisor for all of the six and a half years I have attended VA Tech. Thanks Jill, Hal, Mom, Dad, Bryan, Mandy, Ricardo, Don, and Kevin.

I would also like to thank my committee, because at times they were more than just a committee. Thanks Dr. Leo for the use of your data acquisition system, dSPACE, and for asking me the questions that really made me think. Also, thanks for your support in trying to get the electrical system to work. Although Dr. Belinda King was not on my committee officially, thanks for helping with the controller and ill-conditioned matrices.

# Chapter 1

## 1.0 Introduction

Counterbalancing is a classical problem. Mostly, it's been done by adding masses, off-setting a system mass with another mass creating an opposite moment. Questions such as where to add and how much to add are common design considerations. Statically, mass counterbalancing is an acceptable solution. However, there are dynamic penalties for the added inertia. This thesis explores two different counterbalancing methods, masses and equilibrators.

The motivation for this thesis work occurred while the author was designing a landmine detection scheme that was to be implemented on one of the Virginia Tech Autonomous vehicles. These autonomous vehicles sense and avoid obstacles without any human intervention while driving through a course. One of the main uses of an autonomous vehicle is to work in locations that are unsafe for humans. One such place is a landmine field. If a robot were able to sense landmines, mark them, and navigate around them, the military and civilian population living and working in the area would be much safer. The 2000 team of the Autonomous Vehicle Team (AVT) was charged with this mission.

One preliminary design option was to use a metal detector to sense the landmines. This idea presented some very interesting questions. The metal detector worked best when it was maintained at a six-inch distance from the ground. However, the metal detectors were going to be mounted on a vehicle that would navigate over undulating terrain. If the metal detector were rigidly mounted to the vehicle, the head could crash into the beginning of a hill in the terrain. One solution to this problem was to develop a closed-loop position control system that would keep the head of the metal detector at a fixed distance from the ground, even over hilly terrain.

One of the specified components of the control system was the motor required to raise and lower the metal detector as required by the control algorithm. This posed a bit of a challenge. The metal detector is a heavy sensor head attached to the end of a cantilevered beam mounted on the front of the moving vehicle. The motor would have, as well as the batteries supplying the voltage to the motor, to be able to overcome the gravitational forces acting on the detector.

The first priority with this design was to reduce the driving torque required of the motor through counterbalancing. If this was achievable, the size, and cost, of the motor could be reduced. The first idea that came to mind was to counterbalance the detector by hanging a

weight on the opposite side of the motor from the metal detector. However, this design added inertia to a moving robot. This would mean the motors that drive the vehicle would have to produce more torque to overcome the added weight of the vehicle.

Another solution presented itself after careful thought. What if a spring was used to counteract the gravitational force acting on the detector? This was an interesting idea, but how to implement it quickly became a concern, and a topic for a thesis.

### 1.1 Definition of Equilibration

The spring counterbalance describe above is referred to as an equilibrator. The load element (spring) counteracts the imbalanced static moments in the system to bring the system to equilibrium or a steady state position. “What is an equilibrated system?” Quite simply, an equilibrated system is one in which the mass of the system is counterbalanced by a force element, like a spring or a damper, instead of a mass, as in conventional system. An example of a conventional mass counterbalance system is shown below in Figure 1. The small remote-controlled vehicle carries a pivoted arm with an ultrasonic sensor at one end and a counterbalancing mass at the other end. A drive motor at the pivot point attempts to keep the sensor at a constant distance above the ground by using a feedback control loop.

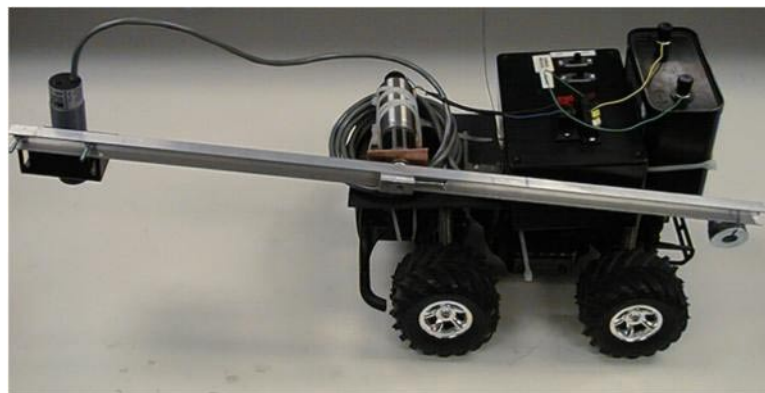


Figure 1: Picture of vehicle carrying a counterbalanced arm

The mass consists of a stack of washers, which balance the weight of the arm and the ultrasonic sensor. The system has a mass counterweight and is statically balanced. This vehicle and sensor arm was developed to prove the concept of a vehicle carrying a metal detector at a fixed distance above the ground. Because the counterweight minimized the drive static torque, the system requires only a small Pittman, six-volt drive motor.

While adding a counterbalance mass is an excellent solution for static and slow speed systems, the added inertia can adversely affect dynamic performance. Alternatively, a counterbalancing system that uses a spring instead of a mass should offer improved dynamic performance. Although this result seems intuitive, no quantitative studies have been found that demonstrate this. It is the aim of this thesis to demonstrate the superiority of spring equilibrators in dynamic applications.

There are many benefits to using spring-equilibrated system over conventional counterweight balancing techniques. One is the reduced inertia added to the equilibrated system. The mass counterweight system almost always adds significant system inertia, while equilibrators add very little to a system. Improved safety may also be a benefit of an equilibrated system. Since the system is balanced, it will not collapse in the case of a power failure [Pons et al, 8]. Another benefit may be the reduced friction of an equilibrators. Many poorly balanced systems include friction in the design to help support the static load [Walsh et al, 16]. An example of this is a poorly designed drafting lamp. The friction in the joints helps hold the lamp at a fixed location. As the lamp is used, the joints become worn and the friction decreases, causing the lamp to sag. In many applications, continual rotational motion is desired and the inclusion of friction is inefficient. Using an equilibrators alleviates the need for added friction.

This thesis explores the possible benefits of a spring-equilibrated system compared to a mass balanced system in a dynamic control situation. Spring equilibrators may offer improved performance in many applications, such as robots, where decreased inertia and fast control are chief design goals.

## **1.2 Literature Review**

Hain [3] was the first to introduce the idea of an equilibrators in 1961. He developed spring mechanisms that balanced a load using a Newtonian force analysis approach. Using graphical methods, he explained the theory for four position balancing and “perfect” planar equilibration through a range of values using springs and odd-shaped pulleys. The term ‘perfect’ refers to the exact exchange of gravitational energy and spring elastic energy. The basic model of a single degree of freedom, planar equilibrators is shown in Figure 2.

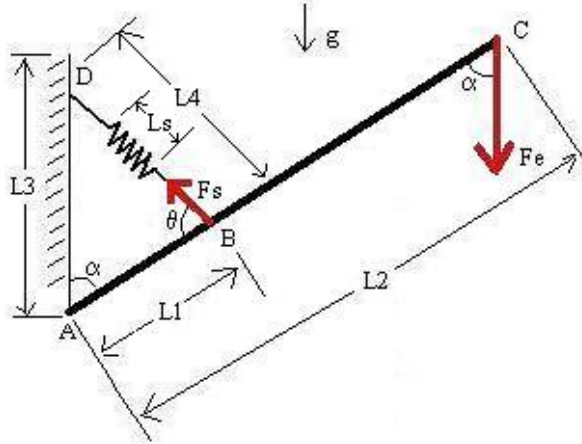


Figure 2: Basic Equilibrator Model

The governing equations are derived by applying a force balance to this model [Nathan, 7]. Taking the moment around point A yields Equation 1, where  $F_e$  is the external force and  $F_s$  is the spring force.

$$F_e l_2 \sin \alpha - F_s l_1 \sin \theta = 0 \quad \text{Equation 1}$$

The spring equilibrator force is  $F_s = k \Delta$ , where  $k$  is the spring constant and  $\Delta$  is the spring extension. Perfect equilibration is possible only when  $\Delta$  is equal to  $l_4$ , and the spring has zero free length. If this assumption is not made, the  $\Delta$  would be equal to  $l_4 - l_s$ , meaning the initial spring length is not equal to zero. It will be shown later how to relax this assumption, but for now the zero free length assumption will be used. Using equation 1 and substituting the spring force and geometry of the triangle ABD ( $l_4 \sin \theta = l_3 \sin \alpha$ ), yields the result in Equation 2.

$$F_e * l_2 = k * l_1 * l_3 \quad \text{Equation 2}$$

Several authors have expanded on the work of Hain. The first important expansion was the development of the self-adjusting equilibration system by R.H. Nathan [Nathan, 7]. In this ingenious mechanism, Nathan uses force feedback to control the geometry of the mechanism. One of the ways he accomplishes this by introducing a sliding joint along link AC, using a pulley system to transmit the external force. Nathan's mechanism is shown in Figure 3. The mechanism is adjusted by equilibrating the external load when  $\alpha$  is equal to ninety degrees. With this condition met, the mechanism can be adjusted to perfectly equilibrate.

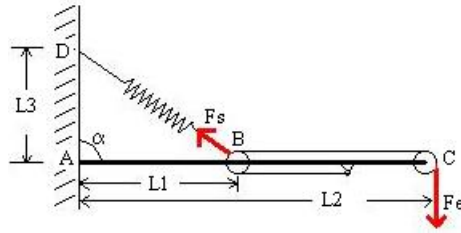


Figure 3: Self-Adjusting Equilibration Mechanisms [Nathan, 7]

Nathan also investigated how to equilibrate the system by adjusting other parameters in such as the length of  $l_1$  and the length of  $l_3$ . With the system geometric properties explored, Nathan then went on to explore substituting a planar, four-bar linkage for link AC. This yielded a parallelogram linkage equilibrator that is used on many devices including drafting lamps and surgical lasers. He also explored how to relax the zero free length spring assumption. He noted that, by putting a tension spring inside a coaxial compression spring, the net deflection of the springs would be zero, thus providing a practical solution to the zero free length assumption. In other words, the positive deflection of the tension spring would offset the negative deflection of the compression spring. He demonstrated this idea on a record player arm shown in Figure 4.



Figure 4: Tension and Compression Spring Equilibrated Record Player Arm

Another technique to relax the zero free length assumption will be presented after the potential energy methodology of analysis is introduced.

Both Nathan and Hain used a Newtonian approach in the derivations of equilibration equations. Soon there was a flurry of activity to develop equilibrator design methodologies using energy methods [Streit, et al, 13]. This method uses equations of the kinetic and potential energy, not forces, to derive the equations of motion. In designing an equilibrator, it is only necessary to look at the potential energy. This quantity needs to be constant

throughout the range of motion, resulting in an exact exchange of the potential gravitational energy and the spring potential energy. The planar case is derived here.

Since the potential energy is constant throughout the range of motion, the following equation has to be true:  $\frac{dV}{d\theta} = 0$ . This equation is the starting point for deriving the equation of motion for the system. Modeling a rod of length,  $r$ , and a spring with a spring rate of  $k$ , the potential energy term is given in Equation 3. Theta is defined from the positive x-axis (different from definition above).

$$V = mgr\sin\theta + \frac{1}{2}k(\Delta)^2 \quad \text{Equation 3}$$

Taking the derivative of this equation gives the static equation of motion for an equilibrator. This is a convenient approach, because it is simple to form the potential energy equation. Many authors use this approach when solving equilibrated mechanisms with revolute joints, but it will later be shown that this approach cannot be used in mechanisms containing prismatic joints [Streit and Shin, 14].

Now that the energy method has been presented, another way to relax the zero free length spring assumption can be introduced. The derivation was developed by Pons, Ceres, and Jimenez [Pons et al, 8], which lead to the quasi-exact equilibration system. Figure 5 shows the basic model parameters used to form equation 4.

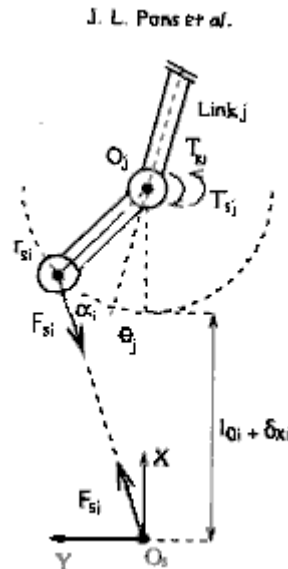


Figure 5: Model Used to Derive Quasi-Exact Spring Equilibration

Pons and his coauthors use energy methods to approximate the potential energy without the assumption of zero free length. The result of the spring potential energy is summarized in Equation 4. Because the zero free length assumption is not made, Equation 4 is very complex and must be evaluated for each configuration of every spring. To determine perfect equilibration, four parameters,  $k$ ,  $r$ ,  $l$ , and  $\delta$ , must be varied to get quasi-exact equilibration for a range of  $\theta$  [Pons et al, 8].

$$V = \frac{1}{2}k(\Delta)^2 = \frac{1}{2}k[r^2 + (r+l+\delta)^2 - 2r(r+l+\delta)\cos(\pi-\theta) + \delta^2 - 2\delta\sqrt{r^2 + (r+l+\delta)^2 - 2r(r+l+\delta)\cos(\pi-\theta)}] \quad \text{Equation 4}$$

Rather than complicate this thesis with approximate equilibration techniques, springs with pretension and the zero free length assumption will be used in all derivations and experiments.

Another practical design consideration needs to be explored, namely, how to best attach the springs to the mechanism to be equilibrated. There are two basic designs: 1) vertical and 2) parallel [Streit and Shin, 14]. Streit refers to the vertical design as one where the spring is attached to ground vertically above the pivot point (as in the case of the derivations up to this point). An example is shown in Figure 6.

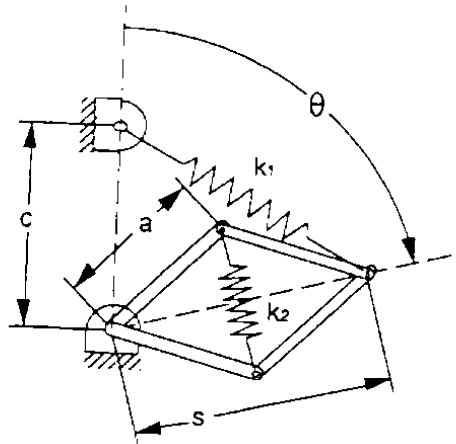


Figure 6: Vertical design example, pantograph [Streit and Shin, 14]

In the parallel design, cables are used to apply the equilibration force of the springs. An example of this design is shown in Figure 7.

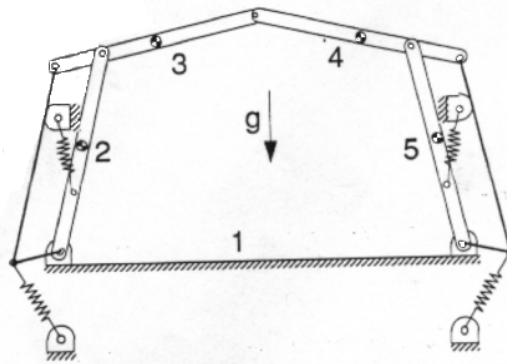


Figure 7: Parallel design example [Streit and Shin, 14]

Streit and Shin point out the benefits and drawbacks of each design. The parallel design should only be used for simple mechanisms where there are few links and multiple links attached to the ground [Streit et al, 14]. This is because each link needs to be equilibrated to ground, either through a cable or directly. One benefit of the parallel design is that it allows the equilibrators to be attached to the ground, so their weight does not have to be equilibrated. However, the vertical system usually has one spring attached to a ground point that equilibrates the entire system. However, this can be a drawback. If the mechanism has many open loop links and each link is equilibrated, the entire mechanism has to be attached to the ground with at least one large spring. The mechanical realization of this is another bearing or shaft in the system. In summary, the parallel design should be used with revolute jointed chains, while vertical designs should be used to reduce the number of spring links in the system [Steit et al, 14].

Up to this point, only equilibrators using revolute joints have been discussed. Through Nathan's work, the question was raised how to equilibrate systems containing prismatic joints, or a sliding joint. A general method for equilibrating mechanisms containing prismatic joints was developed by Streit and Shin [Streit et al, 14]. In this paper, they claim, "all rigid body planar linkages having lower and higher order kinematic pairs can be perfectly equilibrated." They demonstrate prismatic equilibration by balancing the pantograph mechanism shown in Figure 8.

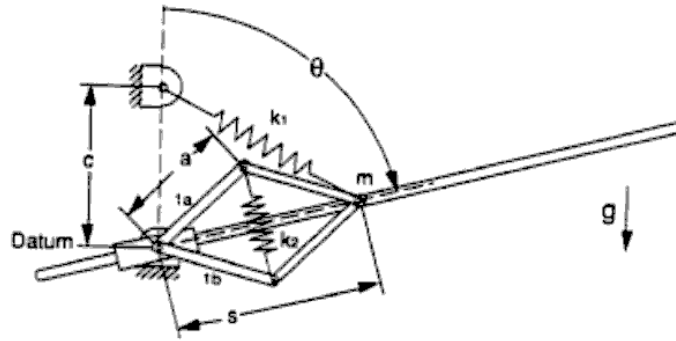


Figure 8: Prismatic equilibration example [Streit and Shin, 14]

Streit and Shin assert that, “Energy is perfectly exchanged between three storage devices (two springs and gravitational potential energy).” The springs  $k_1$  and  $k_2$  store or provide potential energy based on the sliding movement of the prismatic joint and the rotation of the arm.

Work has also been done on spatial mechanism equilibrator design methodology; developing general solutions for two degree of freedom systems [Walsh et al, 17] and equilibrators for Hooke’s joints [Streit et al, 12]. These derivations also used energy methods, but asserting the potential energy of  $\theta$  and another angle,  $\alpha$ , are both zero. The derivation is very similar to the derivation above for the potential energy of  $\theta$  equal to zero. In an effort to quantify results, Shin and Streit [Shin and Streit, 10] performed numerical simulations on an equilibrated pantograph used as legs on walking robots. They performed both dynamic and static simulations to determine the effectiveness of a two dimensional equilibrator designed to reduce the geometric work and the energy lost when the robot is at rest and working against gravitational forces. Shin and Streit showed that there was a ninety percent drop in peak torque. This study demonstrates an equilibrator can be used in a robot to reduce the motor requirements, so that smaller motors can be used. This in turn further reduces the overall inertia of the system.

Since Hain’s original work, there have been many studies of planar and spatial equilibrator designs since he established equilibrator theory. Design methodologies have been developed for devices containing revolute joints [7, 11, 13, 14, and 16] and force feedback mechanisms [7], even extending to use prismatic joints and higher order kinematic joints [14]. Studies have been done to relax the zero-length spring requirements [8]. Investigations into spatial equilibrators include development of methodologies using two degree of freedom equilibrators and equilibrators using a Hooke’s joint [12]. Nevertheless,

there seems to be no literature describing dynamic experiments to investigate the controlled behavior of the equilibrator system.

### **1.3 Project Scope**

The remainder of this thesis will focus on analytical and experimental efforts to quantify the performance of an equilibrator in a dynamic system. It will do this by comparing a mass counterbalance system and a spring equilibrated system. These systems will be modeled, simulated and tested in a closed-loop position control experiment. The results will be quantitatively compared.

The first step to a simulation is to model the system and this is done in Chapter 2. Equations of motion are developed for both systems that include a model of the motor. The motor parameters are measured experimentally by finding the frequency response function. A limited amount of signal processing information is presented to help understand the experiment. Chapter 2 also describes a method for finding an equivalent motor when there is a gear train on the output shaft of the motor.

Chapter 3, further investigates the equilibrator system by using the model derived in Chapter 2. Simulations are used to determine system characteristics such as damping, resonance, and geometric variability. They are also used to compare the linear response versus the nonlinear response. The control loop will also be defined and simulated in this chapter to determine peak torque and speed of response.

The rest of the thesis describes the experiment and presents results and conclusions. The heart of this thesis is in Chapter 4, which describes the experiment setup and results. The test parameters will be established as well as component specifications. Chapter 5 will present the results of settling time and control effort for the experiment. Also, Chapter 5 will present the conclusions and recommendations.

## Chapter 2

### 2.0 System Modeling

The first step in performing the analysis was to model the system. To do this, a thorough understanding of the system needed to be attained. This chapter incorporates two modeled systems, the mass counterweight and the equilibrated system. The motor, used in both systems, was modeled separately and then incorporated into each system. Pictures of the systems are shown in Figure 9 and Figure 10



Figure 9: Countermass System

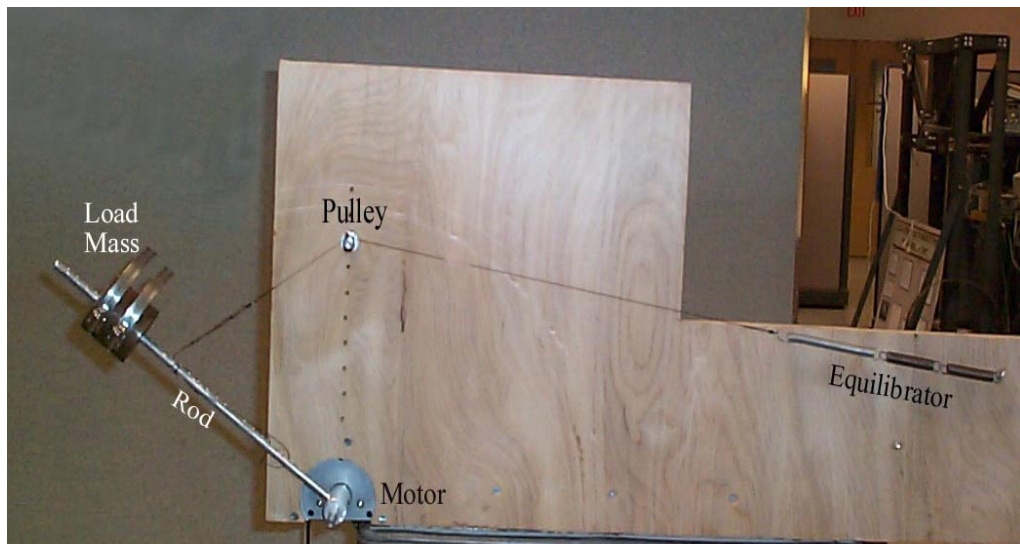


Figure 10: Equilibrated System

From the background established in Chapter 1, the systems are characterized to better understand the similarities and differences. The system shown in Figure 9 uses a traditional form of static balancing. Similarities can be drawn between this figure and the robot in Figure 1. Figure 10 is characterized by a planar, vertical design, equilibration system.

## 2.1 Modeling the Motor

The motor used in this experiment was a brush-type DC gear motor made by Matsushita Electric Industrial Company. The motor with an attached encoder was purchased from a surplus company and no technical information was available on either the motor or the encoder. A breakdown of the motor, gearbox and encoder, is shown in Figure 11.

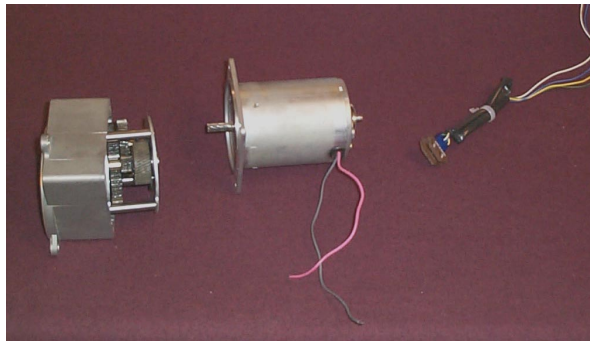


Figure 11: Breakdown of Motor and Encoder

Without technical information, a motor model had to be developed to accurately simulate the system. The model that was used was a three-pole, DC motor. The derivations for the motor equations of motion, the parameter identification, and the equivalent motor model with a gear ratio are described below.

### 2.1.1 Electrical and Mechanical Motor Model

The overall motor model was developed using a mechanical model and a separate electrical model. . The mechanical model was generated using the free-body diagram shown in Figure 27. The electrical model was developed from the circuit diagram describing the shown in Figure 13.

The motor model was developed based on three assumptions. They were 1) that hysteresis is negligible, 2) that the voltage drop across the brushes is negligible, and 3) that the voltage across the air flux gap was equal to the back-emf constant [VT Mechatronics Home Page, 15, and Shetty et al, 9].

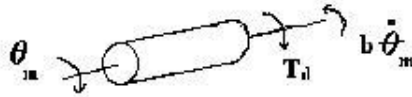


Figure 12: Free body diagram of the mechanical component of the DC motor

The motor mechanical model is developed using the following notation:

- $T_d$  : Developed Torque
- $b$  : System Damping
- $J$  : Mass Moment of Inertia

Summing the torques from the free body diagram yields Equation 5:

$$\sum T = T_d - b\dot{\theta}_m = J\ddot{\theta}_m \quad \text{Equation 5}$$

The torque of the motor is the torque constant,  $k_b$ , multiplied by the current,  $i_a$ , shown in Equation 6.

$$T_d = K_t * i_a \quad \text{Equation 6}$$

This yields the motor mechanical equation of motion, Equation 7.

$$J\ddot{\theta}_m + b\dot{\theta}_m = K_t * i_a \quad \text{Equation 7}$$

The circuit diagram for the electrical motor is shown in Figure 13.

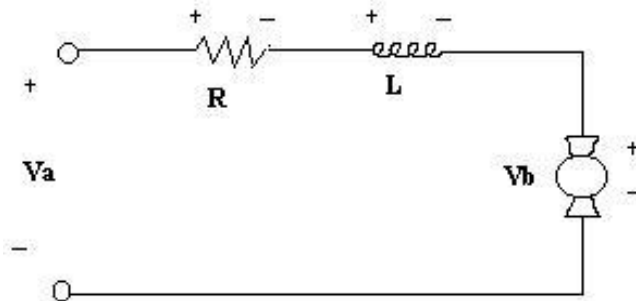


Figure 13: Circuit diagram of the electrical components of the DC motor

Where:

- $V_a$  : Voltage across input
- $L$  : Motor Inductance
- $R$  : Terminal Resistance
- $V_b$  : Output Voltage

Using Kirchhoff's voltage law around this circuit yields Equation 8:

$$L * \frac{di_a}{dt} + R * i_a + V_b = V_a \quad \text{Equation 8}$$

The voltage across the motor windings,  $V_b$ , is defined in Equation 9 using the assumption of constant flux. Upon further inspection, this term is the electrical system damping.

$$V_b = k_b * \dot{\theta}_m \quad \text{Equation 9}$$

Where  $K_b$  is the back-emf constant for the damping in the motor (previously shown in the free body diagram as  $b$ ). The resulting system electrical equation of motion is given by Equation 10.

$$L * \frac{di_a}{dt} + R * i_a + k_b * \dot{\theta}_m = V_a \quad \text{Equation 10}$$

### 2.1.2 Experimentally Finding Motor Model Parameters

With both equations of motion known, the task was to determine the values for the parameters such as  $R$ ,  $k_t$ ,  $k_b$ ,  $L$  and  $J$  (defined above). In order to determine these constants, three tests need to be conducted [VT Mechatronics Home Page, 15]. The first test measures the terminal resistance,  $R$ , of the motor with the use of an ohmmeter. The next test was used to find the back EMF constant,  $k_b$ . Here the motor was run at a constant speed while the generated voltage,  $V_b$ , and speed,  $n$ , were measured using a voltmeter and a handheld tachometer, respectively. A picture of this test is shown in Figure 14.  $k_b$  is defined at the ratio between  $V_b$  and  $n$ . As stated in the literature,  $k_t$  was estimated to equal  $k_b$  [VT Mechatronics Home Page, 15].

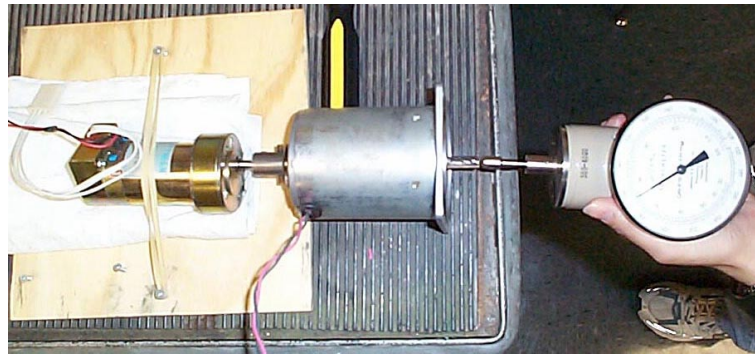


Figure 14: Experiment to Determine  $k_b$ , Back-emf

The final test was conducted to determine the time constants, both electrical and mechanical, of the motor. This was done to be able to back-calculate the two remaining

motor parameters, mass moment of inertia,  $J$ , and inductance,  $L$ . This test required the frequency response function (FRF) of the motor. With the FRF, the break frequencies were found, and by inverting the frequencies, the time constants were determined.

In order to determine the frequency response function, it is necessary to excite the motor through a range of frequencies (input), while measuring the velocity response of the motor (output). Here the response of the motor was the rotational speed of the output shaft, which was measured by a shaft-mounted, DC tachometer. The tachometer was added to the motor by removing the end-cap and machining a coupling to mate the motor shaft and the tachometer shaft. The frequency response function of the DC motor was defined as shown in Equation 11,

$$H_1(f) = \left[ \frac{\text{output}}{\text{input}} \right] = \left[ \frac{V(\text{tach})}{V(\text{motor})} \right]. \quad \text{Equation 11}$$

A Hewlett Packard Dynamic Signal Analyzer (HPDSA) was used to excite the motor and to analyze the motor input and output, providing a coherence value. Coherence is a measure of how well correlated the input and output signals are to each other. Perfect coherence equals one. Because the generated signal of the HPDSA was not strong enough to physically excite the motor, the input signal was first run through an audio amplifier. The amplified signal was then split, and directed to the motor and to Channel 1 of the HPDSA. This signal served as the input, (motor), in Equation 11. The DC voltage output of the tachometer was then sent to Channel 2 of the HPDSA. This served as the output in Equation 11. A photograph and a schematic of the test set-up can be seen in Figure 15 and Figure 16, respectively.

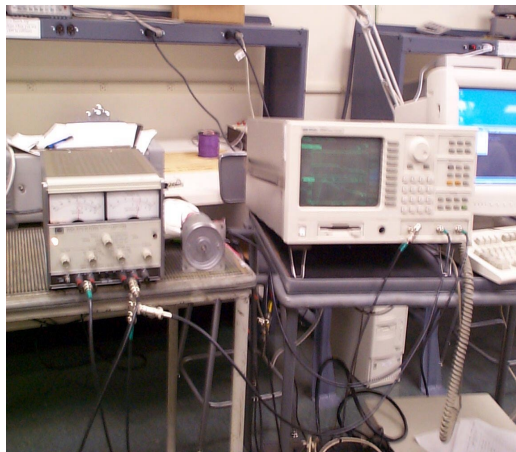


Figure 15: Experimental Setup

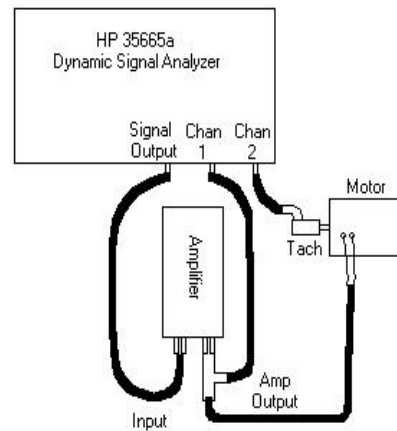


Figure 16: Model of Experimental Setup

The HPDSA offers several different windowing and input functions. To distinguish which to use, some signal processing information must be reviewed. It is sometimes necessary to window the input signal to ensure that it is periodic within the time window. Failure to do have periodic-in-the window input signals could lead to large amounts of leakage when the data is transformed from the time domain into the frequency domain by the HPDSA. Periodic chirp, burst chirp, and fixed sine waves were all inputs that were periodic-in-the-window input functions, however random input was not. Therefore, when random input was used, windows were used to attenuate the magnitude of the small and large frequencies to approximately zero.

There are many tradeoffs to be considered when selecting a time-domain windowing function. While some windows offer high leakage suppression, they may lack in their frequency resolution capabilities. Windows with high leakage suppression capabilities will do well at providing accurate amplitude estimates, while windows with high frequency resolution will do well at estimating frequencies. Often, windows will excel in either leakage suppression or frequency resolution, but not both [Mitchell, 6].

The Hanning windowing function is generally a safe choice. With a low highest side lobe value of  $-32$  dB and a  $-18$  dB/Octave asymptotic roll off, it offers reasonable leakage suppression. The Hanning window also has a narrow noise bandwidth of  $1.5\Delta f$ , providing good frequency resolution. Due to the nature of this window, much of a signal's power is lost at the low and high ends of the window.

Use of the Flat Top windowing function requires the user to weigh its tradeoffs. This window provides very accurate amplitude estimates, but poor frequency resolution. Flat Top offers a very low highest side lobe value of  $-93.6$  dB and  $0.0$  dB/Octave asymptotic roll off, therefore providing very accurate amplitude estimates. However, this functions noise bandwidth is quite high,  $3.77\Delta f$ .

The Uniform windowing function is another window where tradeoffs come into play. This function has low amplitude estimate capabilities and high frequency resolution. The Uniform window's highest side lobe value of  $-13.2$  dB and  $-6.0$  dB/Octave asymptotic roll-off make it a poor choice for amplitude estimates. However, it has a very low noise bandwidth of  $1.0\Delta f$ , making it an ideal choice for frequency estimates.

Using the windows and functions that the HP Analyzer provided, the frequency response function and corresponding coherence were determined for each combination of signal and window. Each window option was applied to each function that was generated. After sifting through the data, it was found the periodic chirp signal windowed with the Uniform window

provided the highest coherence over the broadest range of frequencies. The signal is periodic in the time domain window, producing no leakage. The averaging capabilities of the HPDSA reduce the noise component, making the coherence very close to one. The amplifier's bandwidth and the motor non-linearity at low frequencies cause the coherence to drop below 0.9 at low frequencies. Otherwise, the coherence remains very near 1.0 throughout the entire frequency range. For these reasons the Uniform window was selected as having the best combination of input signal and time-domain window to be used when determining the FRF of the DC motor.

The periodic signal windowed with a Uniform window was generated by the HPDSA, amplified by the audio amplifier, and then sent to the motor. The HPDSA then recorded the input and output signals vs. time, transformed them into the frequency domain, and computed the power spectrum density and coherence of the signals. This process was repeated 50 times, with the HPDSA averaging the power spectrum density and coherence at each iteration.

In Figure 17, the experimental Frequency Response Function (FRF) was compared to a theoretical, or estimated, FRF. The theoretical FRF was determined from a mathematical three-pole model for a motor. The estimates were adjusted until the experimental magnitude results were very close to the estimated results. A discrepancy between the estimated and experimental FRF was discovered in the phase. The phase lag in the experimental data was due to experimental flaws. It took the motor a small amount of time to overcome inertia, as well as static friction, to begin turning. This caused a phase discrepancy in the experimental phase data and actual phase data. But, since the phase of the experimental data follows the trend of the actual data, this explanation seems reasonable.

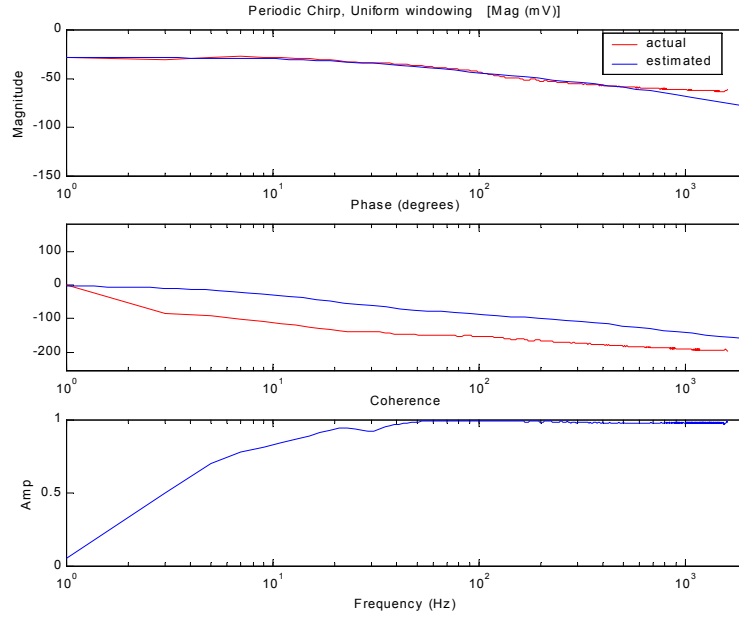


Figure 17: Actual and Estimated Frequency Responses Functions

The time constants were calculated as the reciprocal of the break frequencies, or where the FRF starts to curve down. They were 1/17.825 of a second for the mechanical time constant and 1/750 of a second for the electrical time constant. As stated and shown in Equation 12 and Equation 13, the time constants are used to find J and L. A summary of motor parameters values are given in Table 1.

$$J = \frac{\tau_m (k_b * k_t)}{R} \quad \text{Equation 12}$$

$$L = \tau_e * R \quad \text{Equation 13}$$

Table 1: Summary of motor parameters

Parameter [Units]	Value
Mechanical Time Constant [s]	0.05610
Electrical Time Constant [s]	0.0013333
Gr : Gear Ratio	12.1 / 1
Ra: Terminal Resistance [ $\Omega$ ]	2.240
Kt: Torque Constant [N*m/A]	0.0521
Kb: Back-Emf [V/s*rad]	0.0521
La: Motor Inductance [H]	0.002987
J : Mass Moment of Inertia (w/o gearbox) [kg*m <sup>2</sup> ]	6.7984 e-005

### 2.1.3 Equivalent motor model with a gear reducer

The mass moment of inertia calculated above was for an armature without a gearbox on the output shaft of the motor, but the motor that was used in the experiment has a gearbox. Neglecting the inertia of the gear reducer itself, equivalent output shaft inertia can be found. This is accomplished by equating the kinetic energy of the two systems. A model of the motor system with a gearbox is shown in Figure 18.  $J_2$  is the equivalent inertia at the output.

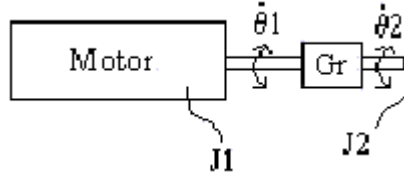


Figure 18: Model of Motor with Gearbox

Where:

$J_1$ : Mass Moment of Inertia of the Motor Only

$J_2$ : Equivalent Inertia of the Motor at the Output

$\dot{\theta}_1$ : Angular speed of Output Shaft of Motor

$\dot{\theta}_2$ : Angular speed of Output Shaft after Gearbox

Equating the kinetic energy before and after the gearbox, gives Equation 14.

$$\frac{1}{2} J_1 \dot{\theta}_1^2 = \frac{1}{2} J_2 \dot{\theta}_2^2 \quad \text{Equation 14}$$

By inspection of Figure 18, the following must be true:  $\theta_2 = \theta_1 * Gr$ . Substituting this relationship into Equation 14, yields the following relationship.

$$J_1 = J_2 * Gr^2 \quad \text{Equation 15}$$

This gives the total kinetic energy of the motor as in Equation 16. An analysis of the assumption to neglect the inertia of the gear reducer is discussed in Chapter 5.

$$T = \frac{1}{2} J_1 (\dot{\theta}_2 * Gr)^2 \quad \text{Equation 16}$$

## 2.2 Modeling the Mass Counterweight system

With the motor completely modeled and all parameters estimated, the model for the mass counterweight system is now developed. The system to be modeled is shown in Figure 21. It includes a load mass,  $M$ , a slender rod with a radius,  $R$  (not to be confused with the resistance of the motor used earlier), a counterweight rod with a radius,  $R_c$ , and a reaction mass,  $M_c$ .

The rods are assumed slender, which means the radius is assumed negligible compared to the length of the beam. This simplifies the calculation of the mass moment of inertia.

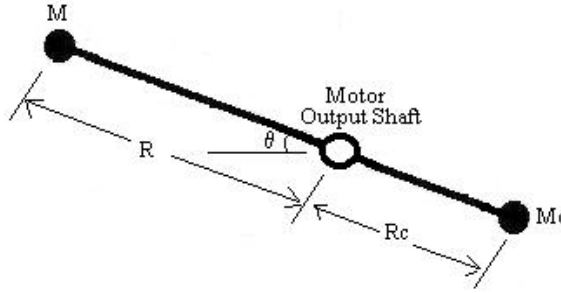


Figure 19: Mass Counterweight Model

Energy methods were used to form the equation of motion for this system. The advantage of this approach over a Newtonian approach is that the system components can be easily incorporated into the system. This will be evident when deriving the equilibrated system.

With this in mind, the kinetic (T) and potential energy (V) equations were formed (Equation 17 and Equation 18).

#### Kinetic Energy Equation

$$T = T_{loadmass} + T_{loadmassrod} + T_{motor} + T_{countermas} + T_{countermasrod}$$

$$T = \frac{1}{2} M (\dot{P} \cdot \dot{P}) + \frac{1}{2} \left( \frac{1}{3} m R^2 \right) \dot{\theta}^2 + \frac{1}{2} J (\dot{\theta} * Gr)^2 + \frac{1}{2} M_c (\dot{P}_c \cdot \dot{P}_c) + \frac{1}{2} \left( \frac{1}{3} m_c R_c^2 \right) \dot{\theta}^2$$

Equation 17

#### Potential Energy Equation

$$V = V_{loadmass} + V_{loadmassrod} + V_{countermas} + V_{countermasrod}$$

$$V = Mg(i \cdot P) + \frac{1}{2} mg(i \cdot P) + M_c g(i \cdot P) + \frac{1}{2} m_c g(i \cdot P)$$

Equation 18

Using complex notation, the position vector locating the load mass is  $P = R e^{i\theta}$ , the position vector locating the counterweight mass is  $P_c = -R_c e^{i\theta}$ . Now, using  $L=T(q)-V(q)$ , the Lagrange equation becomes Equation 19, where q is the generalized coordinate. In this case, q is equal to  $\theta$ .

$$\frac{d}{dt} \left( \frac{\delta L}{\delta \dot{q}} \right) - \frac{\delta L}{\delta q} + \frac{\delta \text{damp}_{\text{Rayleigh}}}{\delta q} = kt \cdot i = \text{Torque of Motor [N m]}$$

Equation 19

Notice the Lagrange equation is set equal to the torque of the motor. This is because the output of the motor acts as a torque onto the system, which must be incorporated into the Lagrange equation. Also, system damping in terms of a Rayleigh dissipation function was included to take aerodynamic drag and other damping losses into consideration. Mathematica was used to evaluate the symbolic equations given above. The resulting equation of motion for the mass counterweight system is shown in Equation 20. As shown, the system is nonlinear in  $\theta$ .

$$\theta''[t] = \frac{-6(gmR \cdot \text{Cos}[\theta[t]] + 2gMR \cdot \text{Cos}[\theta[t]] - gm_c R_c \cdot \text{Cos}[\theta[t]] - 2gM_c R_c \cdot \text{Cos}[\theta[t]] - 2\text{Current} \cdot k_t + 2 \cdot \text{Damp} \cdot \dot{\theta})}{12 \cdot Gr^2 J + 4mR^2 + 12MR^2 + 4m_c R_c^2 + 3 \cdot M \cdot cR_c^2}$$

Equation 20

In order to form a linear controller, such as a standard PID control law, the system must be linearized. In this case, the first two terms of the Taylor's Series expansion are used. The system is linearized about its operating point of theta equaled to zero. The linear equation of motion is the same as above with the (Cos  $\theta$ ) terms equaled to one.

### 2.3 Modeling the Equilibrated System

Modeling the equilibrated system was not as intuitive as modeling the mass counterweight system due to the increased number of components. The equilibrator system consists a massless spring, a motor (same as in mass counterweight system), a load mass, a massless cable, and a pulley as shown in Figure 20. Previous work has included a similar derivation for a system including the mass of the spring. [Streit et al, 14]. The following derivation makes the assumption of a massless spring to simplify the equations.

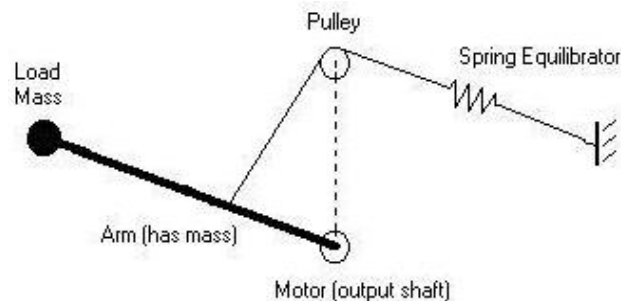


Figure 20: Equilibrator model

The pulley was used to add range of motion as compared to the model shown in Figure 2. Without the pulley, the physical length of the spring would reduce the ability of the system to reach positions near vertical. Although the pulley is added to increase the range of motion, it also adds to the complexity of the equation of motion.

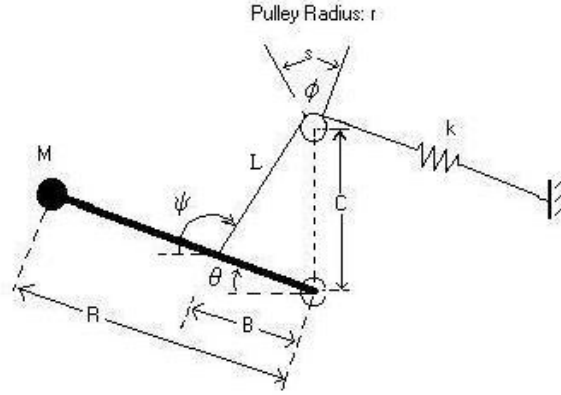


Figure 21: Dimensioned Equilibrator model

Energy methods were again used to derive the equation of motion for the system shown in Figure 21. Expressions for the kinetic ( $T$ ) and potential energy ( $V$ ) are given in Equation 21 and Equation 22, respectively.

$$T = T_{loadmass} + T_{loadmassrod} + T_{motor}$$

$$T = \frac{1}{2} M(\dot{P} \bullet \dot{P}) + \frac{1}{2} \left( \frac{1}{3} mR^2 \right) \dot{\theta}^2 + \frac{1}{2} J(\dot{\theta} * Gr)^2 \quad \text{Equation 21}$$

$$V = V_{loadmass} + V_{loadmassrod} + V_{spring}$$

$$V = Mg(i \cdot P_{loadmass}) + \frac{1}{2} mg(i \cdot P_{rod}) + \frac{1}{2} k(\Delta x)^2 \quad \text{Equation 22}$$

The pulley dynamics are excluded in the direct formulation of the kinetic energy as an approximation to the solution. Since it has a small mass, its absence should be an acceptable approximation. However, the rotation of the pulley,  $\Delta\phi$ , was incorporated later in the formulation of the change in cable length due to the spring.

The unknowns in Equation 21 and Equation 22 are the position vectors and their derivatives as well as the  $\Delta x$  term in the potential energy equation. Modeling the position vectors in the equilibrated system was more difficult. No longer are the vectors just one term as in the mass counterweight system. Now, the position vectors are loops in complex

notation around what is essentially a four-bar linkage. An enlarged view of the four links of the position chain in the equilibrator model is shown in Figure 22.

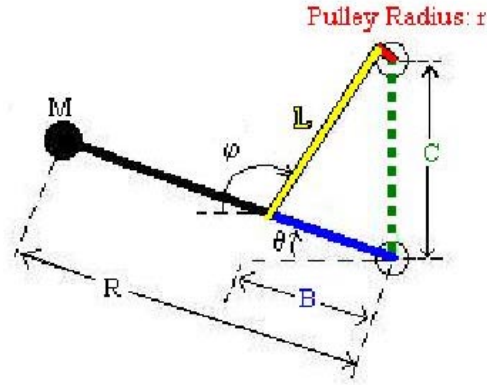


Figure 22: Enlarged Equilibrator Model Showing Four-Link Position Loop

Using the complex notation, the loop equations become:

$$Be^{j\theta} + le^{j\varphi} + jre^{j\varphi} = Cj \quad \text{Equation 23}$$

Where the unknowns were:  $j$  and  $l$ . Breaking Equation 23 into real and imaginary parts and simplifying gives:

$$l \cos \varphi - r \sin \varphi = (-B \cos \theta) \quad \text{Equation 24}$$

$$l \sin \varphi + r \cos \varphi = (C - B \sin \theta) \quad \text{Equation 25}$$

To solve for the unknowns the equations are squared and added to eliminate  $\theta$ . The identity ( $\cos^2 \varphi + \sin^2 \varphi = 1$ ) and the substitution  $E = -B \cos \theta$  and  $F = C - B \sin \theta$  help simplify the calculation.

$$l^2 (\cos^2 \varphi + \sin^2 \varphi) + r^2 (\cos^2 \varphi + \sin^2 \varphi) = E^2 + F^2 \quad \text{Equation 26}$$

$$l = \pm \sqrt{E^2 + F^2 - r^2}$$

Resubstituting for E and F gives:

$$l = \sqrt{B^2 + C^2 - 2BC \sin \theta - r^2} \quad \text{Equation 27}$$

This result is similar to the law of cosines, but with an extra term to account for the radius of the pulley. To solve the position equation for  $j$ , the Equation 24 is used along with the identities to replace sine and cosine in term of the tangent of the half angle. The equations for this are shown below.

$$u = \tan\left(\frac{\varphi}{2}\right)$$

$$\cos \varphi = \frac{1-u^2}{1+u^2} \quad \text{Equations 28}$$

$$\sin \varphi = \frac{2u}{1+u^2}$$

The results of this substitution are:

$$l(1-u^2) - r(2u) = -B \cos \theta (1+u^2) \quad \text{Equation 29}$$

$$(B \cos \theta + l)u^2 + (2r)u + (B \cos \theta - l) = 0 \quad \text{Equation 30}$$

Using the quadratic equation:

$$u = \frac{r \pm \sqrt{r^2 - B^2 \cos^2 \theta + l^2}}{B \cos \theta - l} \quad \text{Equation 31}$$

Substituting u back into the first identity for the tangent of the half angle yields:

$$\varphi = 2 \tan^{-1} \left[ \frac{r \pm \sqrt{r^2 - B^2 \cos^2 \theta + l^2}}{B \cos \theta - l} \right] \quad \text{Equation 32}$$

This result was checked by inputting representative dimensions into the equation and graphing the results. Two roots are obtained; the correct dimension was the smaller u.

This derivation of  $\varphi$  helped define the change in length of the spring,  $\Delta x$ . Looking at the model of the equilibrator, one can see the change in the spring length would be the change of length of the cable over the pulley,  $\Delta s$ , plus the change in length between the pulley and the rod,  $\Delta l$ . For completeness, the initial prestretch of the spring,  $x_i$  was included in the model.

$$\Delta x = x_i + \Delta s + \Delta l \quad \text{Equation 33}$$

The change in the dimension, l, was defined as the final length minus the starting length.

$$\Delta l = l - l(\theta_0) \quad \text{Equation 34}$$

But the zero free length assumption was invoked ( $\Delta l \neq 0$ ), making Equation 34 just equal to l.

Next, the definition of  $\Delta s$  term was tackled. It was defined as the beginning arc length,  $s_0$ , subtracted from the arc length at the desired system position, or equilibrium.

$$\Delta s = s - s_0 \quad \text{Equation 35}$$

Since arc length was defined as  $s = r \phi$ , the question of how to define the change in  $\phi$  arose. This question was answered by realizing the angle  $\varphi$  changes at the same rate as  $\phi$  since the motor is moving all components at the same speed.

$$d\varphi = d\phi \quad \text{Equation 36}$$

With this, the change in arc length,  $s$ , is equal to the change in  $\varphi$  multiplied by the radius,  $r$ .

$$\Delta s = r(\varphi - \varphi_0). \quad \text{Equation 37}$$

Where  $\varphi_0$  was defined as the  $\varphi$  (Equation 32) when  $\theta$  equals starting location,  $\theta_0$ , with an initial cable length,  $l_0$ . The equation for  $\varphi_0$  is shown below.

$$\varphi = 2 \tan^{-1} \left[ \frac{r \pm \sqrt{r^2 - B^2 \cos^2 \theta_0 + l_0^2}}{B \cos \theta_0 - l_0} \right] \quad \text{Equation 38}$$

The initial position,  $\theta_0$ , was solved for using Equation 39

$$\sin(90^\circ - \theta_0) = \frac{r}{C} \quad \text{Equation 39}$$

This equation was derived from inspection of Figure 23. Also derived from Figure 23, was the equation for  $l_0$ . This value was not needed to determine  $\Delta l$  due to the zero spring length assumption, however it was needed to find the correct value of  $\varphi_0$ .

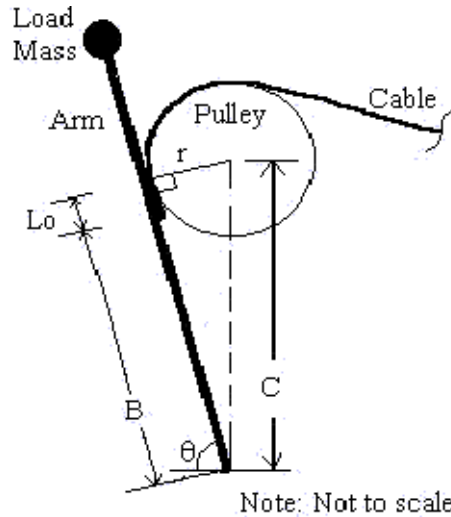


Figure 23: Equilibrator Maximum Position

An expression for  $l_0$  is found from the Pythagorean theorem applied to the right triangle shown in Figure 23. This gives  $r^2 + (B + l_0)^2 = C^2$ . Solving for  $l_0$  gives Equation 40:

$$l_0 = -B \pm \sqrt{C^2 - r^2} \quad \text{Equation 40}$$

Taking the positive value of the square root defined  $l_0$ . It should be noted that, as the radius of the pulley,  $r$ , approached zero, Equation 40 approaches  $l_0=C-B$ . It is important to point out,  $l_0=C-B$ , is only valid if  $B$  is less than  $C$ .

Now that the position vectors and the change in the length are defined, the Lagrange equation can be computed. As with the mass counterweight system, the system damping, in terms of a Raleigh dissipation function, is included in the Lagrange equation (see Equation 19).

Again, Mathematica was used to evaluate the symbolic equations (see Appendix A), and the equations of motion for the equilibrated system are calculated. Due to the nonlinearities, the equation of motion is very complex and long. This system was also linearized using Taylor Series Expansion evaluated at the operating point of theta equals zero radians. The nonlinear and linear equation can be seen in Appendix A.

## 2.4 State Space Model

A convenient way to couple the motor and system equations of motion was to express them in state space form. This mathematical form of the differential equations is derived from the system models. A state is defined as,

“The state of a dynamic system is a set of physical quantities, the specification of which (in the absence of external excitation) completely determines the evolution of the system.” [Friedland, 2]

The general form of state space equations are given in Equation 41. The  $A$  matrix describes the dynamics of the system, the  $B$  matrix described the input to the system, the  $C$  matrix described the output, and the  $D$  matrix represents the direct transmission of an input variable to an output variable. The vectors  $x(t)$  and  $u(t)$  are the state vectors and the input control vectors, respectively.

$$\begin{aligned}\dot{x}(t) &= [A]x(t) + [B]u(t) \\ y(t) &= [C]x(t) + [D]u(t)\end{aligned}\tag{Equation 41}$$

To define the models derived above in sections 2.2 and 2.3, three states were chosen, the position,  $\theta$ , the angular velocity,  $\dot{\theta}$ , and the current,  $i$ . These were input into the state matrix,  $x(t)$ . Next, the equations of motion for the motor and for the system were divided into matrix form using the defined states. The general state space model for the system is shown in Equation 42.

$$\begin{Bmatrix} \dot{\theta} \\ \ddot{\theta} \\ i \end{Bmatrix} = \begin{bmatrix} 0 & 1 & 0 \\ -U & -T & S \\ 0 & -k_b/L_a & -R_a/L_a \end{bmatrix} \begin{Bmatrix} \theta \\ \dot{\theta} \\ i \end{Bmatrix} + \begin{bmatrix} 0 \\ 0 \\ 1/L_a \end{bmatrix} \{V_a\} \quad \text{Equation 42}$$

Where:

U: Positive coefficient of Theta in EOM

T: Positive coefficient of ThetaDot in EOM

S: Coefficient of Current in EOM

V<sub>a</sub>: Control Input Voltage

EOM: Equation of Motion

The output vector requires some system analysis. The only quantity out of the state vector that can be directly measured is the angular position, which is the encoder output times the gear ratio. The C matrix is described in Equation 43. There is no direct transmission of the input voltage that drives the motor, so the D matrix is zero.

$$y(t) = \begin{bmatrix} 1 & 0 & 0 \end{bmatrix} \begin{Bmatrix} \theta \\ \dot{\theta} \\ i \end{Bmatrix} + [0]u(t) \quad \text{Equation 43}$$

With the state space model completed, the mass counterweight and equilibrated systems were completely modeled. In this chapter, the system equations of motion were derived from the system models. Using a systemic approach and simplifying assumptions, the models were developed, numerically solved, and checked against representative values in Mathematica (Appendix A). With the two systems completely modeled and cast in state-space form, more information about the system dynamics was gathered with Matlab simulations done in Chapter 3.

## Chapter 3

### 3.0 System Simulations

In this chapter, simulations were performed on both the mass counterweight system and the equilibrated system to help validate the model. A thorough understanding of the homogenous and dynamic characteristics of both systems was attained using representative dimensional values.

First, the dynamic response of both systems was simulated without the motor to get an understanding of the system dynamics such as speed of response and damping. Next, the system dynamics were simulated with the motor included in the model to determine dynamic characteristics and to help quantify the error. Finally, the proportional, integral, and derivative (PID) controller was designed and simulated.

### 3.1 Mass Counterweight

The mass counterweight had relatively simple equations of motion. Simulations were done to understand the dynamics, and because of the relative simplicity of the equations of motion, the simulations were a way to test the methodology for more complicated systems.

#### 3.1.1 System Properties

The modeled mass counterweight system was analyzed using the Matlab command ‘damp’ on the transfer function derived from equation of motion of the mass counterweight system with the motor. The results of this command were the poles and damping coefficients. A graph of the pole locations is shown in Figure 24. The poles of the system are located on the real axis, and that the system is over-damped. The mass counterweight adds only inertia to the system. Adding dynamic elements like springs to the system would change the overall dynamics and force the pole locations to change. The poles that were close to the origin show the system speed of response is slow.

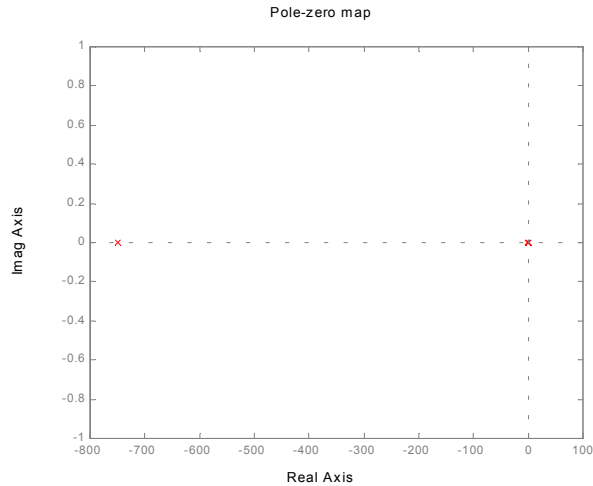


Figure 24: Pole Map of Mass Counterweight System

The open-loop Bode response was plotted in Figure 25. By analyzing the phase margin at the gain crossover, the response showed a marginally stable system. The bandwidth of the system was approximately equal to .03183 Hz (.2 rad/s), which correlates the pole locations and to the slow system response.

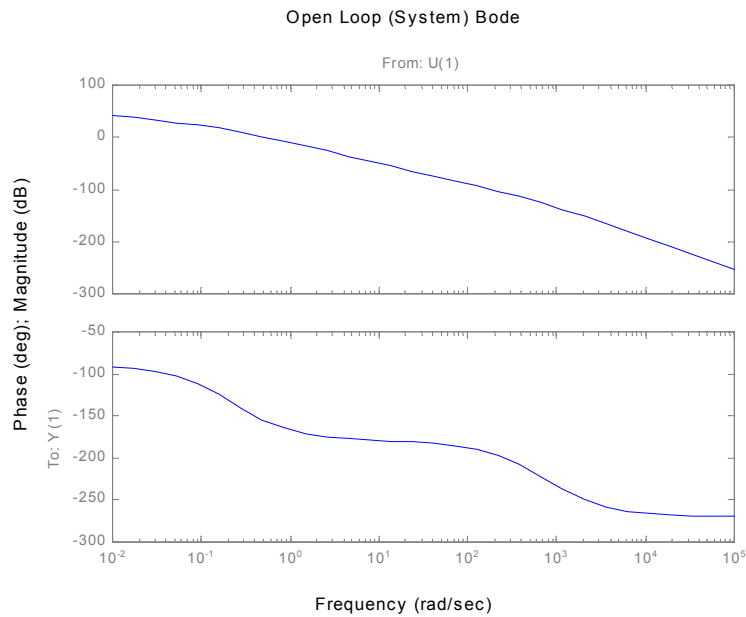


Figure 25: Open Loop Bode Response of Mass Counterweight System

### 3.1.2 Nonlinear and Linear Dynamic Simulations

Next, the system's differential equations were numerically integrated in Matlab to simulate the dynamics of the system. The initial condition of the position state in the 'ode45' function was changed to simulate different starting points of the equilibrated system. The velocity and electrical current initial conditions remained zero. One would expect the mass counterweight system to remain stationary at any given angle, as the opposing mass counterweight moment offset the moment created by the load mass.

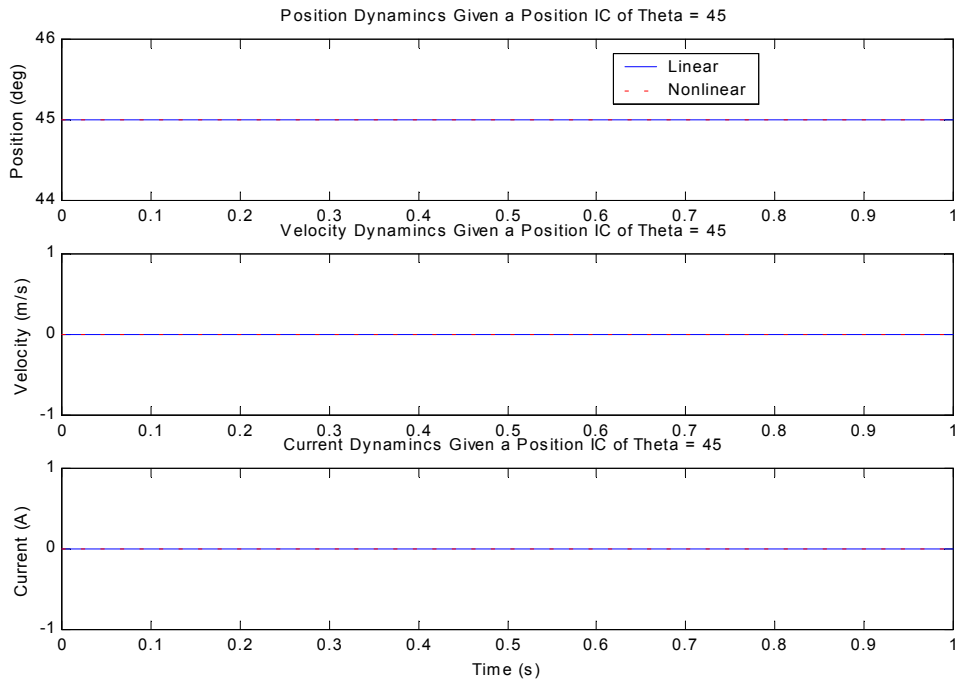


Figure 26: Linear and Nonlinear Dynamic Simulation

Figure 26 shows the results of the numerical simulations for the linear and nonlinear case. Although Figure 26 looks like a static solution, it is in fact a dynamic simulation of the mass counterweight system. It shows exactly what was expected, zero motion given an initial position.

### 3.2 Equilibrated System

As stated in Chapter2, the equilibrated system's linear and nonlinear equations of motion are complex. In the non-linear case, they involve variables embedded in transcendental functions. Even in the linear case, the motion of the equilibrator is not intuitively seen from

the equations. Simulations were necessary for this system to better understand the dynamic response. Dynamic simulations were done through a theta range of forty-five degrees, because the experimental rig was designed to operate in this range.

### 3.2.1 Geometric Relationship

First, the system was simulated to check the geometric relationships derived when the system was modeled in Chapter 2. This was a good first step to understanding the motion of the equilibrated system. And, by comparing the actual system and the modeled system motion, the derivation of the model could be partially validated.

The first step was to write the Matlab code that used the results of the position derivation of the equilibrated system. Using equations Equation 27, Equation 32, and Equation 33, these variables were calculated with about a ninety degree range of theta.

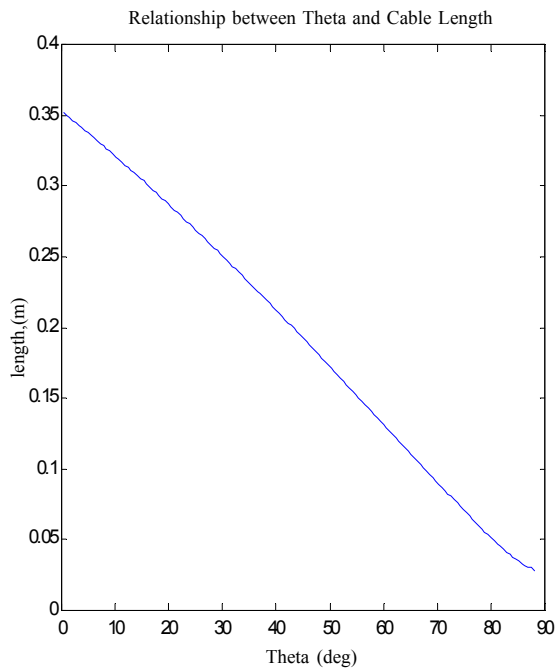


Figure 27: Relationship between Theta and Cable Length

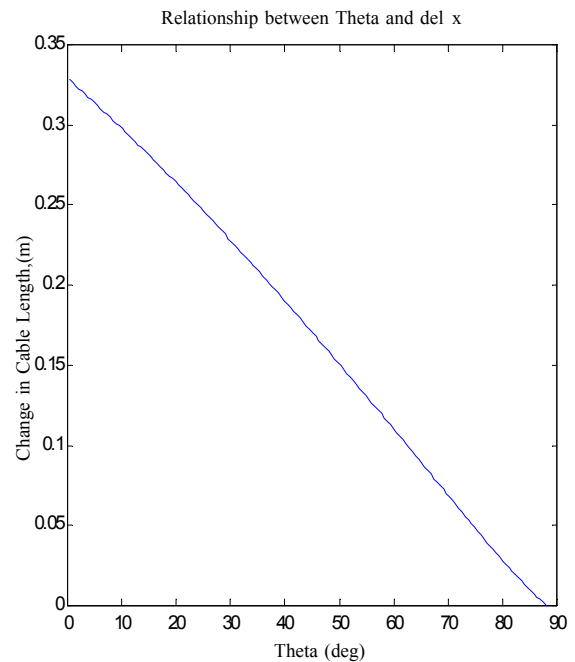


Figure 28: Relationship between Theta and  $\Delta x$ .

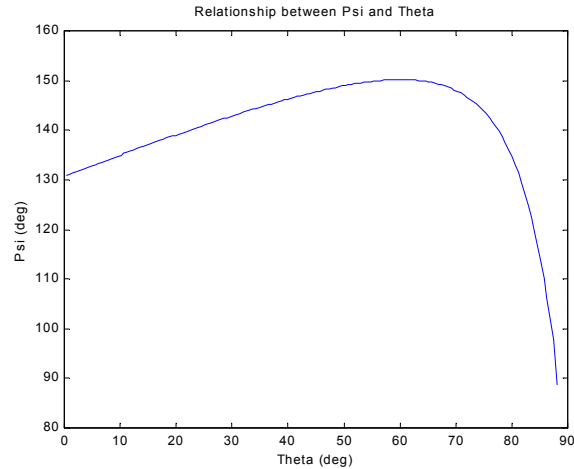


Figure 29: Relationship between  $\varphi$  and  $\theta$

Figure 27 shows the expected trend of increasing cable length as theta decreased. This makes sense because, as the load mass approaches zero, the equilibrator spring deflects and the cable length increase to account for the deflection. Figure 28 shows a similar trend and shows the relative change in the cable length as theta changes. This knowledge helped when designing the equilibrator spring in Chapter 4. The numerical difference in Figure 27 and Figure 28 was the inclusion of the initial cable length,  $l_0$ . In Figure 29, the relationship between  $\varphi$  and  $\theta$  are also expected. As  $\theta$  decreases,  $\varphi$  increases, and the length of cable around the pulley,  $\Delta s$ , decreases, until the angle became such that the length of cable around the pulley changes. With these expected results, the model derivation was partially validated

### 3.2.2 Homogeneous Simulation

As another test to validate the system, the dynamic response of the homogeneous system was simulated. This meant the motor was uncoupled from the system to achieve zero external torques acting on the system. This was done in the Mathematica code by setting the Lagrange equation equal to zero and evaluating the equations. Then, the Mathematica equations were substituted into Matlab and numerically integrated using the 'ode45' technique.

Several tests were performed to validate the model. One was to let the radius of the pulley go to zero. This produced the equation for 'perfect' equilibration as derived in Chapter 1. One of the key features of the 'perfect' equilibration system was the coefficient of theta in the state space representation was zero. This meant the spring was perfectly counterbalancing the load mass. Then, the radius was reinstated into the equations and numerically approximated. This test showed that the coefficient of theta was not equal to zero. After some investigation, it was found

that the coefficient of theta would never go to zero if the pulley radius were nonzero. With the small numerical coefficient of theta, there was a small numerical error in the simulations. This manifested itself in the response of the system. Starting at a range of values for theta produced slight variation in the system's equilibrium position. This was because of the sensitivity of the numerical integration technique to the initial value of theta. Table 2 shows the range of perfectly equilibrating spring constants for a given a set of initial conditions. With a spring constant range of around 6 N/m, the error was not very severe. These results were done by a trial and error method until the spring constant value equilibrated, or produced a flat response (as in the mass counterweight system) in the linear case.

Table 2: Numerical Simulation Spring Constant Results for a Given Set of Initial Conditions

<b>Spring Constant [N/m]</b>	<b>Initial Conditions [Theta(degrees), ThetaDot]</b>
224.79688	[0, 0]
225.92	[9, 0]
227.434	[20, 0]
231.9	[45, 0]

### 3.2.3 System Properties

With confidence in the model, the system was simulated to determine parameters such as speed of response, resonance, and damping by determining the pole locations of the system. The system dimensions, as defined in Chapter 2, are described below in Table 3

Table 3: Equilibrated System Dimensions

<b>System Dimensions [Units]</b>	<b>Value</b>
B [m]	.140
C [m]	.220
r [m]	.00635
k [N/m]	Varies with initial conditions
R [m]	.3935
M [kg]	1.65
m [kg]	.29

As with the mass counterweight system, response was determined using the Matlab command ‘damp’ on the transfer function derived from equation of motion of the mass counterweight system with the motor. The pole locations of the system are shown in Figure 30.

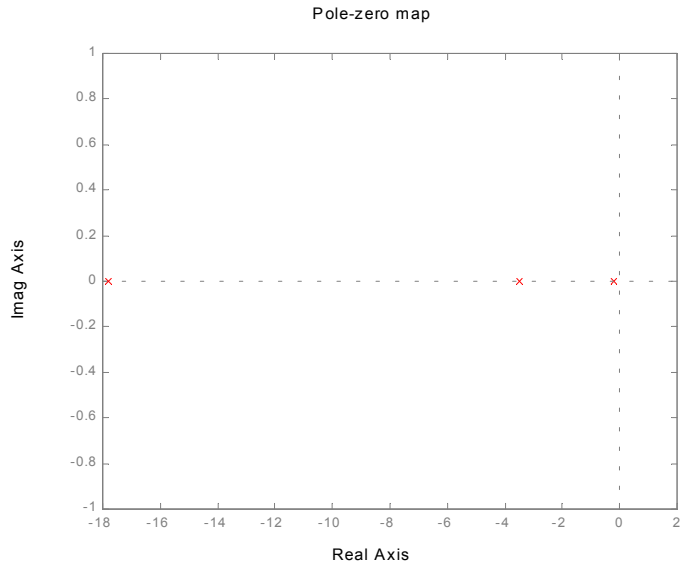


Figure 30: Pole Map of the Equilibrated System

There were two poles very close to the imaginary axis, suggesting a very slow response and very low damping. This was also shown in the open loop bode response in Figure 31. The system has a bandwidth up to .159 Hz, a very slow response. This information was important later when designing the controller.

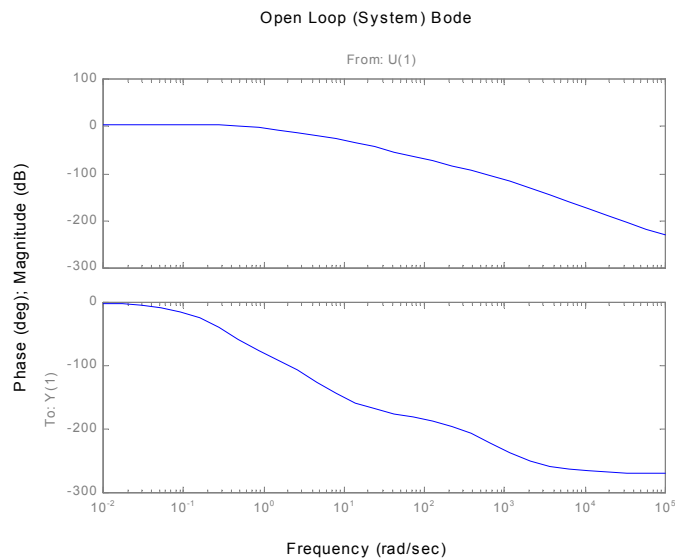


Figure 31: Open Loop Bode Plot of Equilibrated System

### 3.2.4 Nonlinear and Linear Dynamic Simulation

With the system properties approximated, the dynamics were simulated with the external torque to see what the open loop behavior of system would be. Several key questions were answered. One important question was, “How did the linear assumption affect the dynamics of the system?” Recall the system was linearized using Taylor Series Expansion, as mentioned in Chapter 2, around the position, theta equal to zero. How would the system respond when theta was something other than zero?

As expected, the maximum error due to linearization occurred at the maximum simulation angle of theta equal to forty-five degrees. This was found by changing the initial condition of the position state in the ‘ode45’ function to simulate different starting points of the equilibrated system. The velocity and current initial conditions remained zero, and the next figures show the results of the numerical simulations for the linear and nonlinear case.

When the position initial condition was equal to zero, the linear and non-linear responses were equal. This occurred because the equations were linearized around the value theta equal zero, as shown in Figure 32. This result was obtained using a spring constant value equal to 224.79688 N/m. The small error in the position response was due to the numerical errors caused by the radius of the pulley. The jagged shape of the current response of the motor was due to numerical precision in Matlab, and was very close to zero.

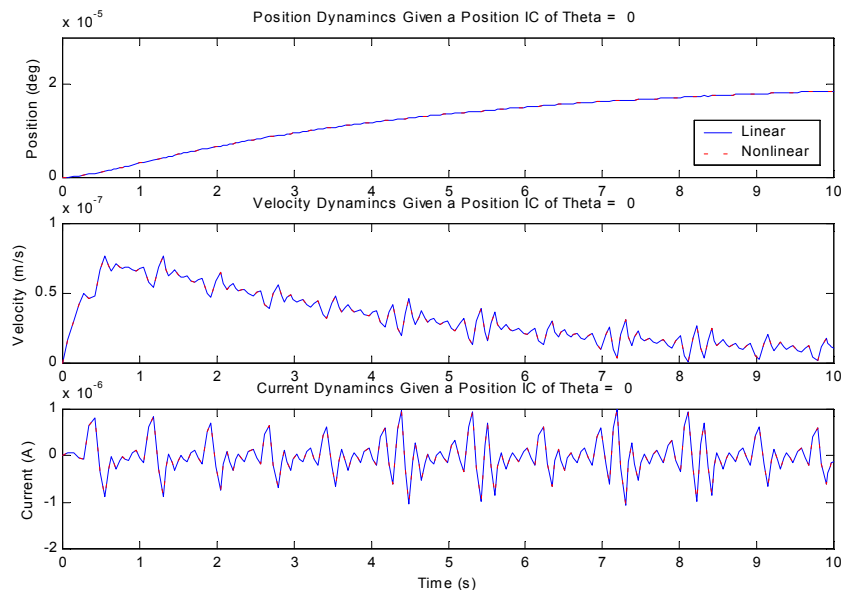


Figure 32: Dynamic Equilibrator Response with IC of Theta=0

The difference in position response due to the linearization was found by simulating the response with an initial condition of theta equal to forty-five degrees. The plot in Figure 33 showed a large difference of about ten degrees in the linear and non-linear response using a spring constant of 230.39.

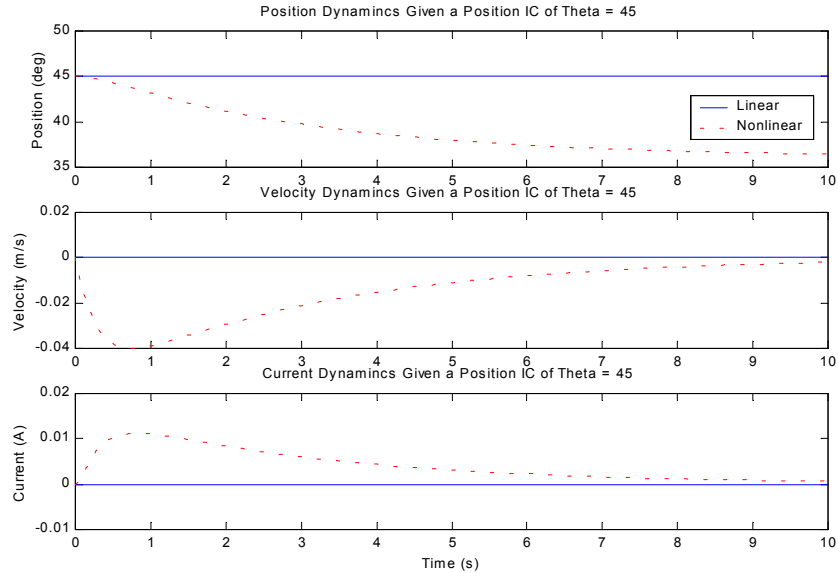


Figure 33: Dynamic Equilibrator Response with IC of Theta=45

To account for this trend, experiments were designed to start at forty-five degrees and end at zero degrees, because the position error due to the linear assumption would be corrected by the end of the experiment. This position error at the beginning of the run would later account for the difference in the control effort of the simulation versus the experimental control effort.

### 3.3 Controller Simulations

Now that the system responses were fully explored, it was time to design the system that would control the position of the load mass in a closed loop. It was decided to start with a simple PID controller, because of the easy implementation into computer software and the relatively few floating-point operations performed by the computer. This reduces the effect of the processing speed, making the simulations as close to ‘real-time’ as possible. Future studies into control of equilibrated systems could use more complex controllers, like a linear quadratic regulator (LQR), which require more calculations and longer processing time.

When simulating the system, special consideration is given to the system constraints of the digital signal processing board called dSPACE® board (explained in greater detail in Chapter 4).

One of the chief design constraints of the controller is the peak control voltage has to be kept under ten volts due to the internal electronics of the dSPACE® card. This is the only hard-fast constraint, but the overall goal of the controller is to minimize settling time of the systems while minimizing the control effort. Since the control voltage increases as the speed of response of the system increases, this is easier said than done, and a delicate balance needs to be found to meet the design goals.

### 3.3.1 PID and Digitization Review

A PID controller is a controller with the basic Laplace form as shown in Equation 44. It consists of a proportional gain,  $K_p$ , an integral gain,  $K_i$ , and a derivative gain  $K_d$ .

$$H(s) = K_p + K_d s + \frac{K_i}{s} \quad \text{Equation 44}$$

Each gain has different effects on the response of the system. The proportional gain acts as an amplifier by multiplying the input signal by the  $K_p$  value. The integral gain,  $K_i$ , affects the steady state error. And, the derivative gain,  $K_d$ , minimizes overshoot. Designing the controller means picking these three gains.

The controller is implemented on a computer so PID realization and digitization effects have to be considered. Digitization is the process in which a continuous system in the  $s$ -domain is converted into the discrete  $z$ -domain. There are several techniques to convert the systems, but the most common way is to use a zero-order hold. This technique assumes a constant value, a zero-order polynomial, when extrapolating the digital input [Franklin, et al., 1]. The digitization process takes the first data point as a constant. The next data point is then taken and the difference in value resulted in a step. This has a destabilizing effect by introducing a time delay into the system.

The delay has to be taken into consideration when converting the continuous PID controller, the equilibrated system, and the mass counterweight system into digital systems. The digitization process of the controller and both systems is easily implemented in Matlab. The 'c2d' command digitizes the system with an input specification of a zero-order hold (zoh) described above.

The sampling period is also an input, and a value of 0.001 corresponding to a 1000 Hz sampling rate is used. This sampling rate is the same sampling rate of the digital signal processing board, called dSPACE®, explained in greater depth in Chapter 4. The error due to sampling at 1000 Hz was negligible, because the sampling rate is much faster than the system response. This can be seen by the very small steps in the simulated response of the controlled systems, shown later in this chapter.

### 3.3.2 Mass Counterweight System Controller

Figure 34 shows the closed-loop control simulation of the mass counterweight system in block diagram form. The feedback is the position of the encoder, while several of the variables are output to the workspace in Matlab for plotting. The control voltage is closely analyzed to avoid damage to the dSPACE<sup>®</sup> board by exceeding the ten volts. Once again, the need for an accurate model is realized. Without this, it would be impossible to get an accurate estimate for the control voltage.

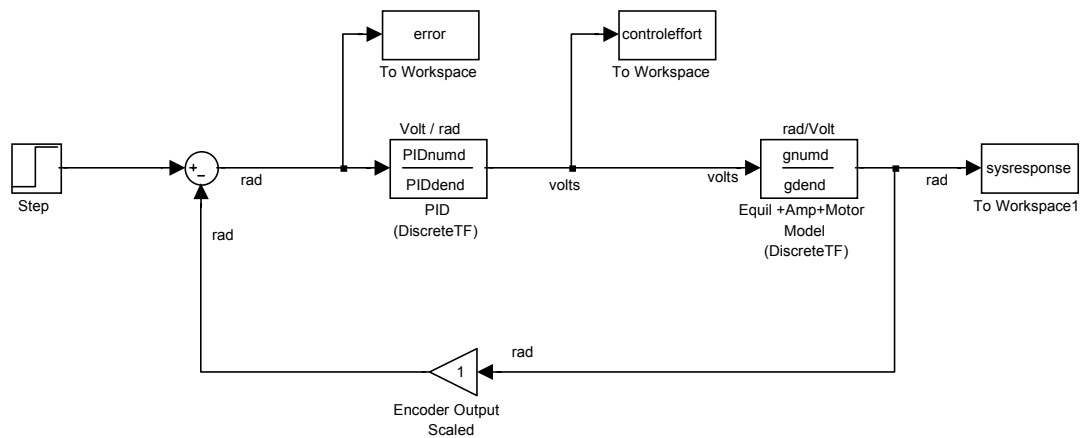


Figure 34: Simulation of Controlled Mass Counterweight system

The PID controller transfer function is found by varying the gains to achieve the desired response. The dominant design constraint is the 10-volt maximum on the control voltage, shown in Figure 35, although settling time is another design parameter. The values for the PID gains are elected to be  $K_p = 5.20$ ,  $K_d = .035$   $K_i = 3.33$ . The simulated response is shown in Figure 36. As mentioned previously, the effects of sampling are not noticeable as the continuous and digital response fell on top of each other.

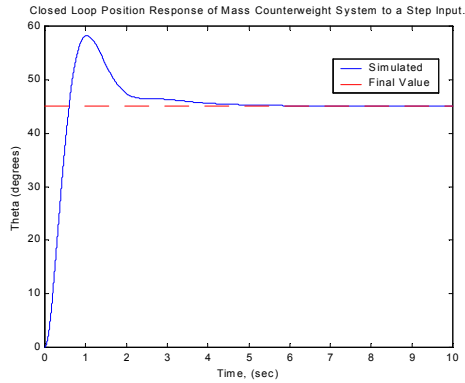


Figure 35: Closed Loop Position Response of Mass Counterweight System to a Step Input

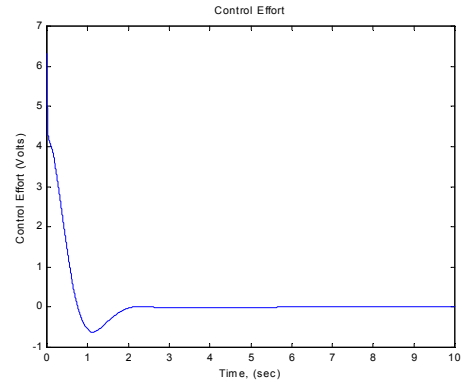


Figure 36: Control Voltage of Mass Counterweight System Equilibrated System Controller

The same methodology and same gains used to design the mass counterweight controller are used to design the equilibrator controller. The same Simulink block diagram, shown in Figure 34, is used, but the equilibrator model is inserted in the place of the mass counterweight system. Also, the same controller gains are used to form the basis for comparison of the two systems. The response of the system is shown in Figure 37 and the control effort is shown in Figure 38.

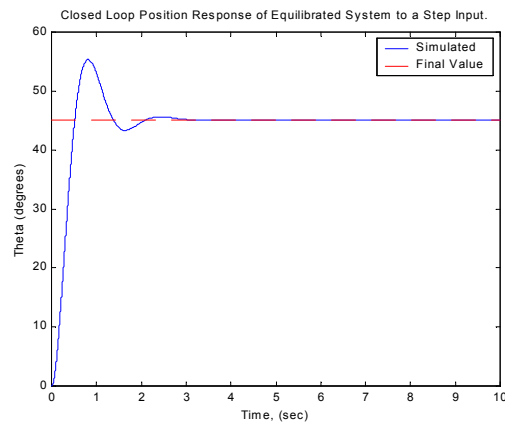


Figure 37: Closed Loop Position Response of Equilibrated System

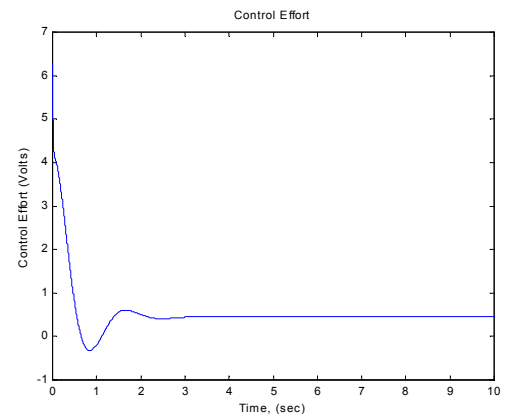


Figure 38: Control Voltage of Equilibrated System

### 3.3.3 Comparison of Simulated Systems

Several interesting observations are drawn from the simulated systems. First, the overshoot is higher in the mass counterweight system, and the settling time is slightly longer. Another interesting comparison is in the final values for the control effort. The expected result would be

to have the control effort go to zero as the system approached the desired position, in this case zero degrees. However, the final value for the control effort of the equilibrator is around 0.4 volts. An explanation for this is the presence of the radius of the pulley in the equation of motion. With the numerical error caused by the pulley radius, the simulation does not ever reach a position error of zero; therefore, the controller is always requiring voltage to reach the desired position.

In this chapter, the systems were simulated to determine dynamic responses. Many different aspects were analyzed, such as the ‘perfect’ response of the mass counterweight system, the imperfect response of the equilibrated system, and the controller simulations.

## Chapter 4

### 4.0 System Experiment

This section describes the experimental setup to test the modeled systems of Chapter 2. It includes more details of the mechanical hardware of the equilibrated system as well as the setup of the electrical components. Also, the collection of experimental data is explained in a step-by-step process. The goal of this section is to accurately explain the setup so this experiment can be replicated with ease.

#### 4.1 Mechanical Hardware Setup

The goal in the experimental setup is to provide a comparison between the position control for each system. Therefore, when the systems are built, the dimensions, weights, and materials are required to be similar. In fact, the resulting systems use several common components, including the motor, the backboard, and the rod coupling.

The mass counterweight and equilibrator systems were built with common items. The rods as well as the rod/motor coupling are made out of aluminum. The masses at the ends of the rods are made of carbon steel. Finally, the motor, pulley, and spring attachment are rigidly mounted with 10-32 screws to a wooden backboard.

There were some special design considerations when the equilibrated system was constructed. First, since the equilibrated system was constructed before the final decision was made on the load mass and the spring constants, the system dimensions had to be adjustable. There are several adjustments the system design to account for this. One way is to mount the load mass to the rod using clamps, which allows for fine adjustments in the position of the load mass. Also, the attachment point of the cable to the rod is made adjustable by drilling a number of holes along the rod. Holes in the wooden backboard serve as adjustment points for the pulley height.

As mentioned in Chapter 1, pretension springs are used to realize the zero-length spring assumption in the derivation of perfect equilibration. The springs are chosen from a given stock in the Smart Materials Lab at Virginia Tech on a trial and error basis. One spring needs to have a large deflection due to the size and range of motion of the experimental setup. The spring constants,  $k$ , are unknown and had to be determined from testing. First, the preload was taken out of the springs by hanging a weight big enough so there was deflection in the spring. Then, more weight was added and the deflection measured. The springs were attached in series, reducing the

equivalent spring constant. After testing, the equivalent spring constant was found to be 228.9 N/m. This value is in the range of the simulation results from Chapter 3.

The final special consideration is the cable, which is made out of fishing leader wire. This type of cable has minimal stretch, which helps prevented experimental errors due to the unmodeled effects.

With the materials selected, construction of the systems began. The final dimensions of the equilibrated system are summarized in Table 4., The final dimensions of the mass counterweight system dimensions are summarized in Table 5.

Table 4: Final Equilibrator System Dimensions

<b>System Dimensions [Units]</b>	<b>Value</b>
B [m]	.23495
C [m]	.263525
r [m]	.00635
k [N/m]	228.9
R [m]	.336555
M [kg]	1.3608
m [kg]	.2268

Table 5: Final Mass Counterweight System Dimensions

<b>System Dimensions [Units]</b>	<b>Value</b>
R [m]	.33655
R <sub>c</sub> [m]	.33655
M [kg]	1.34
M <sub>c</sub> [kg]	1.34
m [kg]	.2268
m <sub>c</sub> [kg]	.2268

## 4.2 Data Collection

There were many ways to obtain data from a system. Typically, a motor controller is used and the position data is collected from an encoder through a computer. Another way is to design a controller in a software package, convert the code to assembly code so that a micro-controller could implement closed-loop control. In this case, the assembly code is downloaded to a digital signal processor (DSP), which is a mathematically efficient microprocessor. The DSP is

implemented in a data acquisition system called dSPACE<sup>®</sup>. This software has a user interface called ControlDesk<sup>®</sup> and uses the DSP to collect data from a variety of inputs, such as a tachometer, an encoder or a voltage potential, just to name a few. In this experiment, encoder feedback is used. The version of the DSP board is the 1102. A 16-bit input is used, giving the board a resolution of 1.5259 e-4 volts.

In order to perform the closed loop control, Matlab and Simulink are again used. Instead of using them for simulations as in Chapter 3, these programs are used to provide a control signal into the system. The Simulink block diagram is shown in Figure 39.

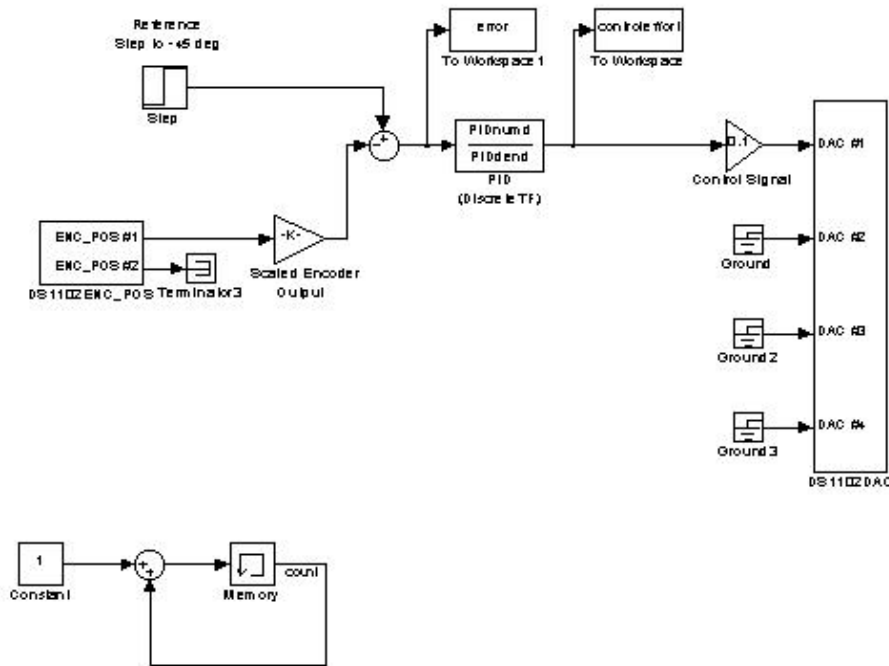


Figure 39: Simulink Block Diagram Showing Closed-Loop Control of Systems

Some special blocks are added in Simulink when a dSPACE<sup>®</sup> card is installed. Two of these blocks are the interfaces between the digital-to-analog converter on the card and the encoder position block. These are used as inputs and outputs for the controller. One nuance of the dSPACE<sup>®</sup> digital to analog (DAC) output was that it needed to be divided by ten. The same PID controller derived from simulations is used again as the controller in the experiment. It is required to run the Matlab script that uses this block diagram to load the PID controller parameters into memory. The loop that appears in the bottom left of Figure 39 was a loop that was later used by ControlDesk<sup>®</sup>, the user interface of dSPACE<sup>®</sup>. It was simply a counter for each simulation step. Using the block diagram in Figure 39, the real-time workshop (RTW) in

Simulink converts the block diagram into assembly code. As soon as the code finishes assembling, the processor starts outputting the control voltage. This creates a problem that was addressed later in ControlDesk<sup>®</sup>.

After the simulations are complete to ensure reasonable control voltages (explained in Chapter 3), the experiment is run using ControlDesk<sup>®</sup>. As mentioned above, the processor immediately output a voltage after the RTW real-time workshop in Simulink is finished. This is addressed in ControlDesk<sup>®</sup> by including a ‘radio button’ in the layout and assigning the variable Simstate to it. A picture of the control window is shown in Figure 40. Also shown in this figure are streamed values of the control signal and the position of the load mass as the experiment is in progress. The counter loop mention above and shown in Figure 39 is used to ascertain the simulation loop count. When the pause button is hit, the loop count goes to zero, and the processor is reset to time equal to zero. This allows transient data to be recorded from time equals zero. This procedure was previously unknown to the users in the lab.

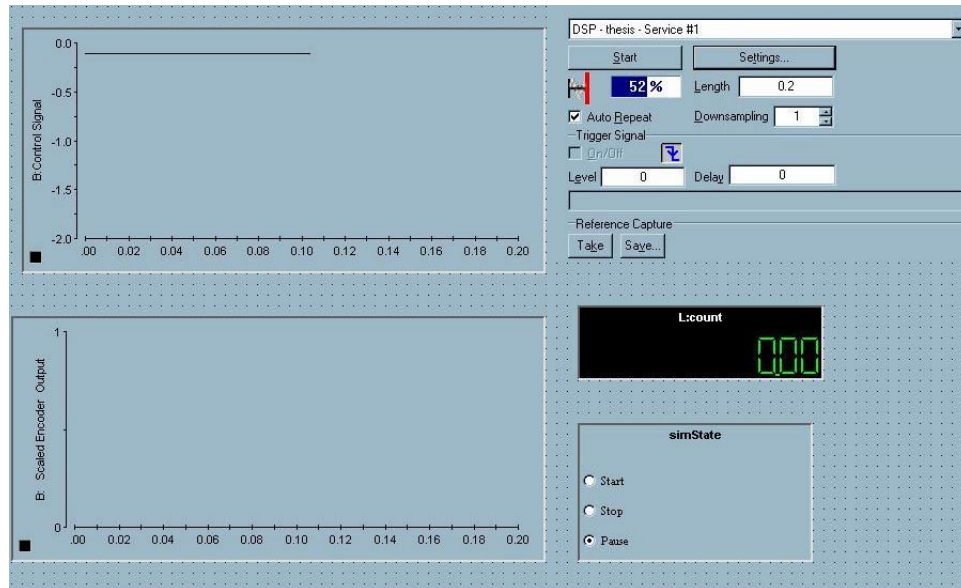


Figure 40: ControlDesk<sup>®</sup> Layout

To obtain the data, ControlDesk<sup>®</sup> is switched into animation mode and the start button on the ControlDesk<sup>®</sup> Layout window is pressed. The term ‘layout’ is a designation used by the producers of ControlDesk<sup>®</sup> to describe the interface window. The length button on the layout controls the amount of data collected. This is how the data is to be collected.

### 4.3 Electrical System

The only step left to get a working experiment is to complete the setup of the electrical part of the experiment. This system is used for both the mass counterweight system and the equilibrated system. In other words, the motor, dSPACE<sup>®</sup>, and the encoder loop has to work together. The electrical system is shown in Figure 41.

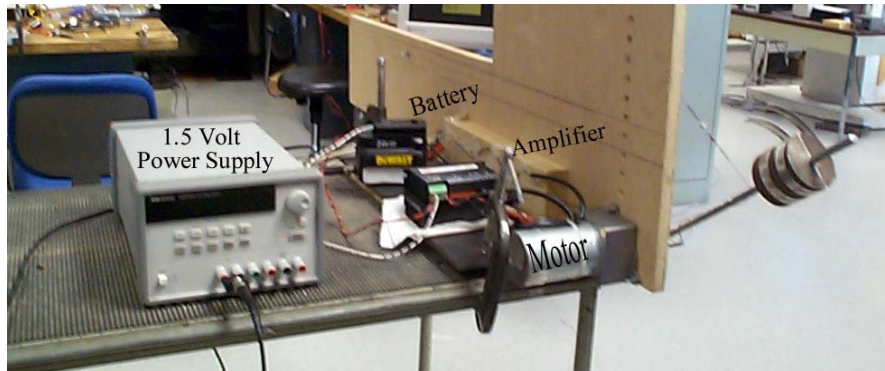


Figure 41: Electrical System

This setup includes obtaining technical information about the encoder and implementing it for use as sensor feedback for closed-loop position control. It also includes getting the motor and amplifier to interpret and act on the control voltage sent by dSPACE<sup>®</sup>.

#### 4.3.1 Encoder

The encoder is on the output shaft of the surplus motor with a model number: Hewlett Packard HEDS 9100. This was found by dissecting another motor with a broken output shaft. After a brief search on the web, technical information is found that described this encoder to be a dual channel, quadrature encoder. This meant that two LEDs (light emitting diodes) provide two square wave outputs that are ninety degrees apart, meaning direction as well as position can be ascertained. Also found in the technical information is the wiring diagram. The wiring diagram is shown in Table 2.  $V_{supply}$  was the five-volt supply that the encoder used to run the LEDs.

Due to the proximity of the experiment set-up to the computer with dSPACE<sup>®</sup>, a cable was needed to attach the encoder to the dSPACE<sup>®</sup> controller board. This is an external box that accepted three different types of inputs and outputs, namely, BNC cables, RS-232 cables, and 15-pin cables. It is shown in Figure 42.

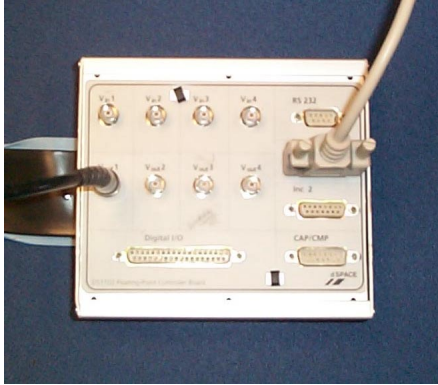


Figure 42: dSPACE® controller board Setup for Experiment

In the experiment, an encoder is used as input (15-pin cable) and the output is the control signal (BNC cable). The dSPACE® manual dictates encoder inputs use the 15-pin connector and supplied the wiring diagram. A summary of this diagram and the 15-pin cable is shown in Table 6.

Table 6: Cable Pin Out

Cable to dSPACE®		
Pin #	Color	Signal
1	Brown	Vsupply
2	Red	Chan A
3	Orange (solid)	Diff Chan A
4	Yellow	Chan B
5	Green	Diff Chan B
6	Dark Blue (solid)	Index (not used)
7	Purple	Diff Index (not used)
8	Grey	Digital Ground
9	Brown (striped)	Not Used
10	Black (striped)	Digital Ground
11	Green (striped)	Digital Ground
12	Sea Green	Digital Ground
13	Pink	Digital Ground
14	Black	Digital Ground

Table 7: Encoder Pin Out

Encoder	
Color	Signal
Yellow	Chan B
Blue	Vsupply
White	Chan A
Green	Ground

The only hurdle is determining what the differential signals on channel A and B are, and whether or not an index signal is needed. After consultation with technical support at dSPACE®, it is determined that this particular encoder did not support the index function, although a differential signal is needed. It was explained that the differential input is a 1.5 volt DC signal used by the DSP logic to compare the channel signals to determine a high or a low in the encoder square wave. This DC 1.5 volt signal is provided by a DC power supply made by Hewlett Packard, Model E3631 A. It also can be provided by a voltage divider circuit shown in Figure 43.

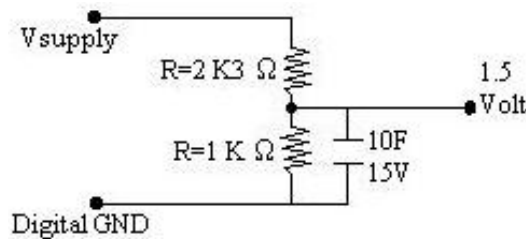


Figure 43: Voltage Divider Circuit Specified in dSPACE® Manual

Now, the encoder is operational, but not quite accurate. Also in the manual for dSPACE®, is a scaling factor. The internal logic of dSPACE® uses a 24 bit counter, but scales the input to be  $\pm 1$ . However, the output needs to be incremented in radians. So, the dSPACE® manual suggested scaling factor shown in Equation 45. Also, note that the gear ratio is included in Equation 45,. Actual velocity is 12.1 times greater (the gear ratio) than the velocity reported by the encoder. The division by 4 is included because dSPACE® pulsed four times for every high voltage read.

$$\text{Encoder Scale Factor} = \frac{2^{21} * 2\pi}{100 * Gr} / 4 \quad \text{Equation 45}$$

With this factor defined, the encoder is now fully implemented into the system.

#### 4.3.2 Amplifier and Battery

With the sensor feedback operational, the next step is to implement the control signal via the BNC cable from the dSPACE® controller board into the experiment. This is easier said than done. The first question is how much amperage can the DSP board provide, and how much amperage does the motor need in order to function. Preliminary tests are done on the motor to see what range of amperage is required. This is done with the DC power supply mentioned above. The input voltage is stepped up until the motor output shaft barely turned. Motion begins at about six volts, and requires about 1.2 amps. With the minimum requirements established,

another calculation is done to determine the maximum requirements. On the end-cap of the motor, it is written DC 22V. It was taken this was the rated voltage. With this and with the measured terminal resistance (Chapter 2.1.2) of 2.24  $\Omega$ , Ohm's law ( $V=i*R$ ) is used to determine a maximum amperage of 9.8 amps. It is determined that the DSP board could not output this amperage, so a power amplifier is needed.

With this determination made, the search began for an amplifier that could produce at least 1.2 amps, and as much as 10 amps. The amplifier that is chosen was a Copley Controls Corporation, base model 423, DC brush servo amplifier. The technical specifications indicate that a maximum peak amperage of 20 amps can be provided at 24-180 VDC. This is a powerful amplifier, but more information is needed to fully understand the nuances of the amplifier.

The first step is learning how to incorporate the amplifier into the system. After some trial and error and technical support, it is determined that this amplifier needs to run in voltage mode. This meant a control voltage was input into the amplifier, and the amplifier would output a proportional voltage at higher amperage. A resistor is added to achieve this mode of operation of the amplifier. The value for the resistor was determined by Equation 46, given by Copley Control.

$$Rh10 = \frac{Gain(Rh3)}{ScaleValue} \quad \text{Equation 46}$$

Where:

Rh10: Added Resistor

Rh3: Reference Input Resistor (already in amplifier- 100 k $\Omega$ )

Gain: Input Voltage from Battery (24 V) divided by  
Input Voltage of Control Signal (10 V)

Scale Value: Amplifier Model Dependent (equal to 20 for model)

To add this resistor, the amplifier is opened and components identified. This is shown in Figure 44. To help future experimenters, the component layout is specified in this thesis. First, the bank of fixed resistors, including Rh10, is on the left hand side with the inputs facing the user. It is above the blue, 15-turn potentiometers. On the bottom right, a green screw terminal is the input from the battery (red/black and white/black striped wires) and the output to the motor (pink and black wires). The mud colored connector jumpers pins 2, 5, 11, 12, and 13 together as ground, as well provides the positive lead (pink) of the control signal coming from the dSPACE<sup>®</sup> controller board in pin 4. All the wiring is followed off the technical specifications downloaded from [www.copleycontrols.com](http://www.copleycontrols.com). A resistor value of 15k $\Omega$  is used, which configures the amplifier with an overall gain of three.

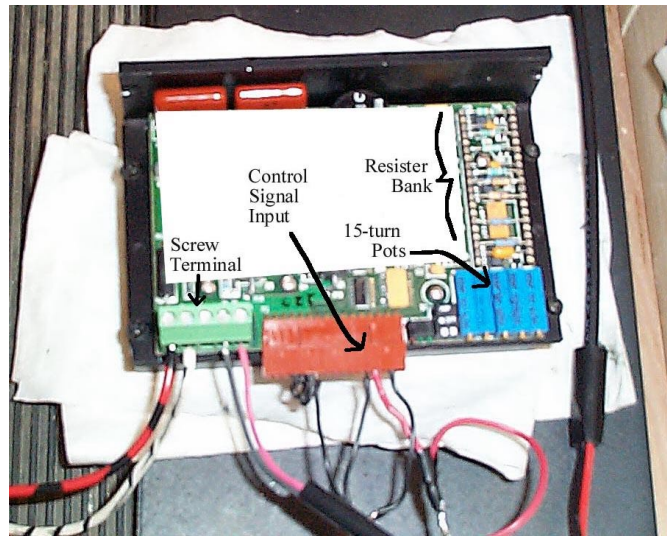


Figure 44: Inside the Copley Control Corp. Amp

One of the nuances of the amplifier is the high frequency response. It is determined from the experimental results, explained in Chapter 5, that the speed of the response of the amplifier is much faster than the speed of response using the gain of three. Again, talking with the technical support solves this discrepancy. The amplifier, when acting in voltage feedback mode, has a filter circuit that acts as a low pass filter, excluding all frequencies above 159 Hz. So, when the experiment starts, the control voltage must ramp up slowly to stay in voltage feedback mode. However, this was not the case with the experiment in dSPACE<sup>®</sup> explained above. The dSPACE<sup>®</sup> processing card is commanded at 1000 Hz. When this happened, the amplifier no longer acts in the voltage feedback mode because there is no effective feedback voltage due to the low band-pass filter. It temporarily transitions from the voltage mode to a current mode. The current mode has a 2 Amp/Volt gain which had a much faster speed of response of 1.2 kHz than in the voltage mode of 159 Hz. To account for the amplifier response at the beginning of the experiment, a higher amplifier gain is used in the model, which gave the systems a faster speed of response.

The gain of the amplifier is determined by taking the time response of the input (the control signal) and output (motor voltage). A white noise signal windowed with a Hanning window was used as the input to the amplifier, and the output response and coherence was measured. Although a multi-frequency signal is not needed, it is used as a best guess. The time response of the input and output are compared and an average ratio of 26.7 is determined. So, this is the value used for the amplifier gain.

With this information, the amplifier is almost configured. The last steps are to adjust the blue potentiometers (pots), switch the white dip-switches located to the left of the blue and connect the battery. According to technical specifications, the reference gain, tachometer gain, and integer frequency potentiometers, are turned until fully clockwise. The loop gain pot is turned counter-clockwise. Also, the dip-switches are set to the off position, which is up. The battery that supplied the amplifier (through the red and white striped wires) has to provide the power that the system required. A rechargeable Dewalt, 24V, NiCd battery is chosen.

With all the components of the system configured as explained above, position data could be collected and the mass counterweight and equilibrated systems could be tested.

# Chapter 5

## 5.0 Results and Conclusions

In this chapter, the experimental results are gathered, analyzed, and compared. The first goal is to compare the position response of both systems using the same controller. In this way, a direct comparison of each system can be made. Then, a controller for each system is designed to get the optimized results while staying under the ten-volt maximum D-Space output signal explained in Chapters 3 and 4. This is done to determine if one system outperformed the other in terms of overshoot and settling time. Finally, the experimental results are compared to the simulated results from Chapter 3.

## 5.1 Experimental Results

The results are obtained from running the experiment detailed in Chapter 4. As mentioned above, each system is first tested with the same controller that was designed from simulations. The gains that were used were:  $k_d = .035$ ,  $k_i = 3.33$ , and  $k_p = 5.20$ . The output of ControlDesk<sup>®</sup> is a \*.mat file that is imported into Matlab and plotted. The results are shown in Figure 45.

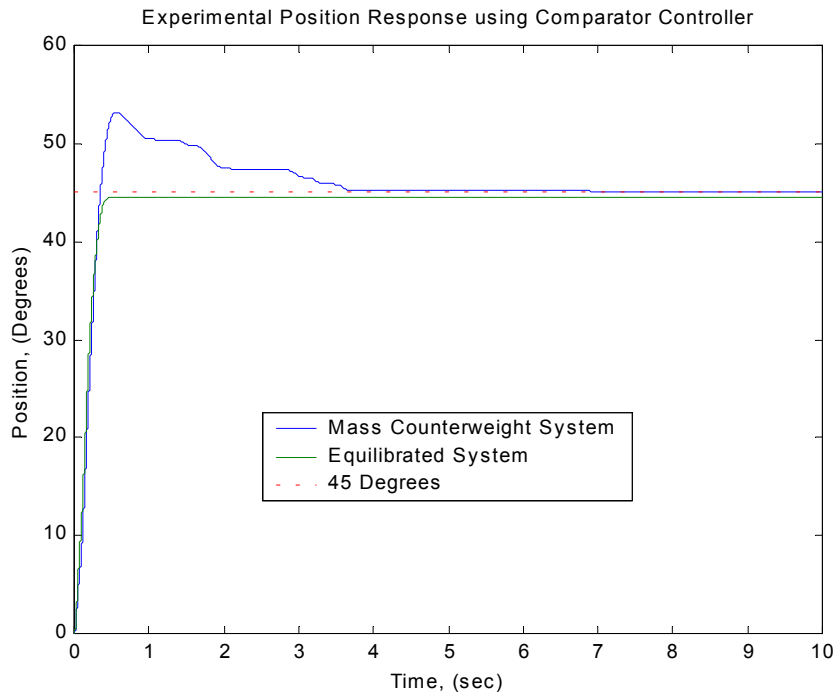


Figure 45: Experimental Position Response using Comparator Controller

By analyzing Figure 45, one can see the mass counterweight system has a higher overshoot than the equilibrated system and takes four seconds to settle to the final value of forty-five degrees. The equilibrated system reaches the final value in fractions of a second and has no overshoot. However, there is a slight steady state error of a degree in the equilibrated system. This is a promising result; the equilibrated system has a better overall position response, despite the small steady state error.

## 5.2 Experimental Results Using Optimized PID Controller

But, the question remains: Can the mass counterweight system response surpass the equilibrated system response with a different set of controller gains? To check this, a variety of gains is tested and the best results are graphed in Figure 46. The gains with the best results were:  $k_d = .05$ ,  $k_i = 5.73$ , and  $k_p = 8.20$ .

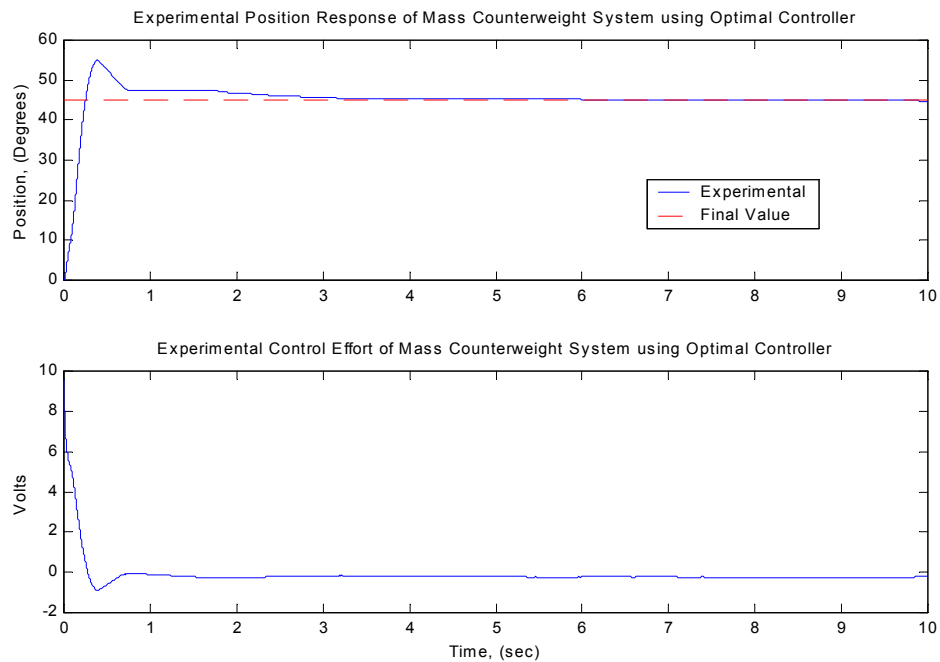


Figure 46: Experimental Results of Mass Counterweight System using an Optimized PID Controller

Several interesting points arise when examining Figure 46. First, the overshoot is minimized but the settling time increases slightly. This raises the question of which performance criterion is more important to the system, minimizing settling time or overshoot. The answer to the question is reached by considering the intended application of the equilibrator in the land-mine scanning

vehicle. It would not be acceptable to have the metal detector head height vary too much. This could lead to the head crashing into the ground and setting off a landmine. Or, by going in the opposite direction, the metal detector head could go out of its optimized operating position, lose effectiveness, and miss detecting a landmine. Either possibility leads to the conclusion that minimizing overshoot is more important for this example, and the gains tested would lead to the ‘optimized’ position response of the mass counterweight system.

The same process to find optimized gains is tested on the equilibrated system, even though the results are very good with the comparator controller. However, the full range of the control effort, 10 volts, is not used with the comparator controller, and the question remains if the response of the equilibrated system can be improved with a different set of gains. The gains are varied and the ‘optimized’ gains are found to be:  $k_d = .06$ ,  $k_i = 2.73$ , and  $k_p = 7.20$ . Results with these gains are plotted in Figure 47.

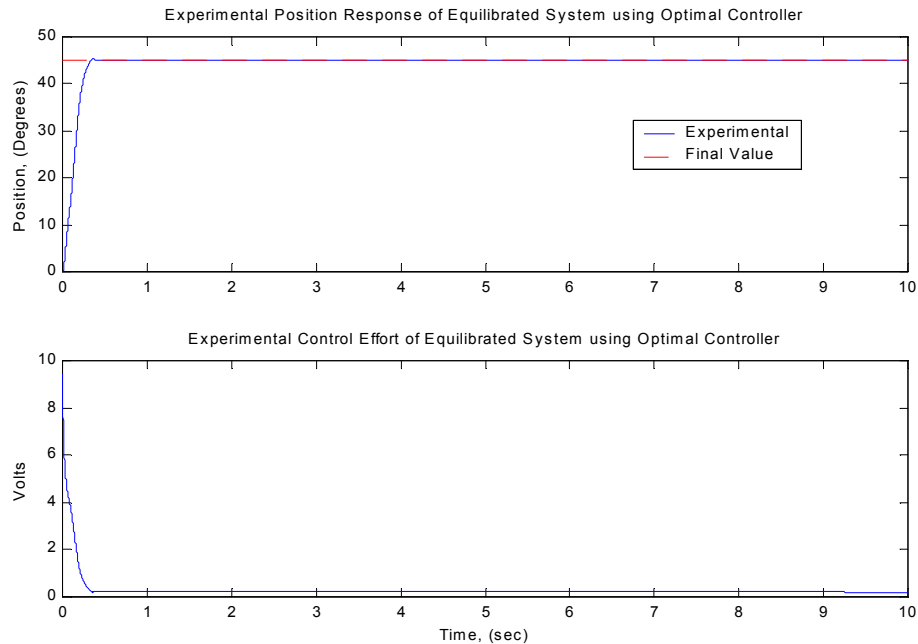


Figure 47: Experimental Results of Equilibrated System using an Optimized PID Controller

These gains prove to be excellent. The slight steady state error of one degree using the comparator controller is gone, the full range of the control effort is used, and the rise time of the response is improved slightly.

It should be noted that in Figure 46, the control effort shows a slight negative voltage, and in Figure 47, the control effort showed a slight positive voltage. It is not known why there was this discrepancy, but one explanation could be resolution error in the DSP board.

By finding the optimized set of controller gains for each system, a global response comparison can be made. Even with the best set of gains in the mass counterweight system controller, the equilibrated system significantly outperforms the mass counterweight system. With this question answered, the optimized controllers are no longer used, and the comparator controller is employed to further compare the system responses.

### 5.3 Comparison of Experimental and Simulated Results

The next question is, “How accurate are the simulated results compared to the experimental results?” This is an important question to answer for future studies in this area. If the simulations are accurate enough, they can be used to predict the system responses, instead of having to assemble and run an experiment. To answer this question, the simulated results of Chapter 3 are compared to the experimental results gathered using the comparator controller. The mass counterweight results are shown in Figure 48 and Figure 49

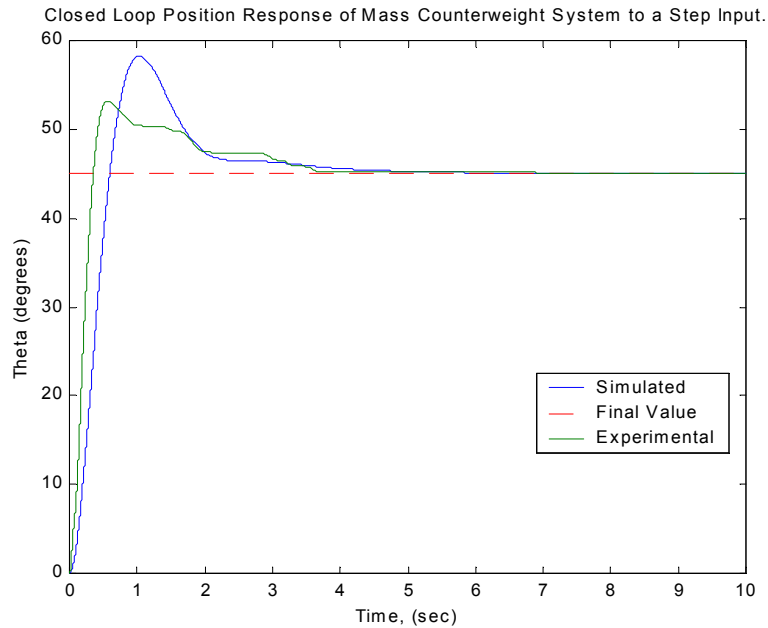


Figure 48: Closed Loop Position Response of Mass Counterweight System to a Step Input

It can be seen in Figure 48 that the trends in the responses are similar. There are slight discrepancies in the rise time, overshoot, and settling time, but in all cases, the simulated response is the conservative estimate of the response. This means that the simulations can be used to get a

'ballpark' estimate of the response, and the estimate would be a 'worst-case' scenario for the response. The reason for the discrepancy is probably un-modeled, non-linear effects in the motor.

The control effort of the mass counterweight system, shown in Figure 49, has the same kind of variations between the simulated and experimental results. In this case, however, the simulated results show the voltage approaching zero, whereas the experimental voltage shows a steady state offset. Therefore, the simulation is not a conservative estimate, but it is a good estimate of the overall range of voltage.

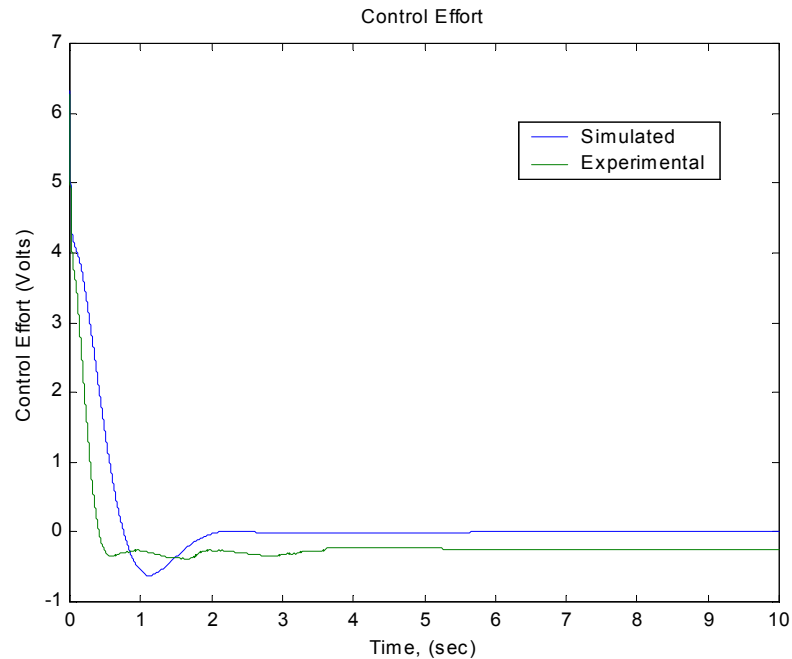


Figure 49: Control Voltage Comparison of Mass Counterweight System

The simulated and experimental results are also compared for the equilibrated system. This is important to determine model accuracy. As previously stated, this system is more complex to model, and due to the inclusion of a pulley radius in the equations of motion, there are numerical errors in the dynamic simulations. It is important to determine the magnitude of variation in the simulated results versus the experimental results.

In Figure 50, a comparison of the equilibrated system results is graphed. The key features are the simulated overshoot of the system versus the experimental result of no overshoot and a slight steady state error. As with the mass counterweight system, the unmodeled dynamics of the motor could be one of the reasons for the discrepancy. Other reasons could be error due to the linearization of the model, the chosen operating point for the model (linearization of the model around zero), and the simplifying assumption to neglect the pulley dynamics. Another reason for

the overshoot in the simulation could be the assumption of neglecting the gear inertia. By adding the inertia of the gear reducer, the overshoot in the simulations would be reduced. These factors, though logical, increase the possible error in the model and therefore the accuracy of the simulated results. However, the simulated results are a conservative estimate of the system response.

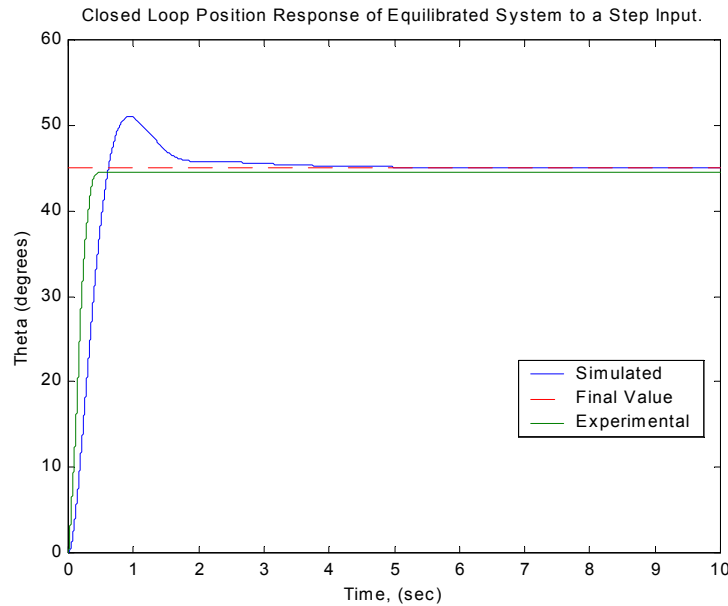


Figure 50: Closed Loop Position Response of Equilibrated System to a Step Input

The equilibrated control effort, shown in Figure 51, was similar to that for the mass counterweight system. The experimental voltage is higher, in an absolute sense, at steady state compared to the simulated result. However, as in the mass counterweight system, the simulations prove to be a good estimate of the magnitude of the final voltage.

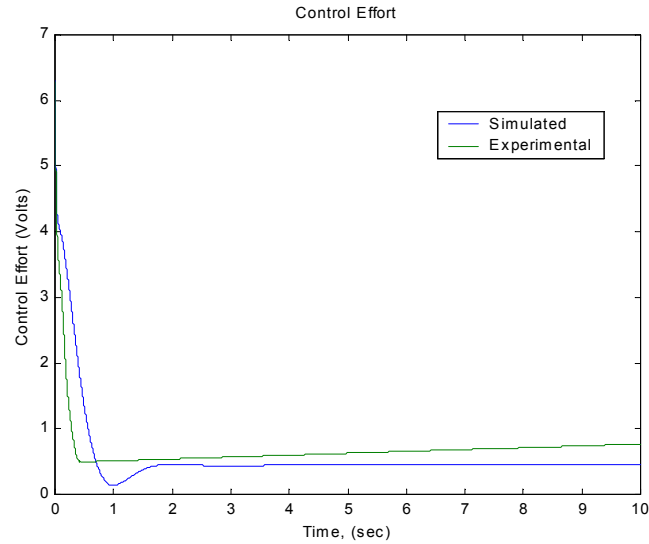


Figure 51: Control Voltage Comparison of Equilibrated System

## 5.4 Conclusions

Through the explanations of the previous chapters, the two systems, the mass counterweight and the equilibrated systems are researched, modeled, simulated, and the controlled responses tested. The work presented includes a literature review, derivations using energy methods, dynamic simulations in Matlab, construction of the testing apparatus, and collection and analysis of experimental data. Throughout all of the analysis, the question of which system was better was at the forefront. The answer to the question is, although the mass counterweight system is commonly used and easier to model, the equilibrated system provides far better dynamic performance and is easier to control. The equilibrated system: 1) reduces the inertia of the system, which was highly desirable for robotic applications, 2) has a fast speed of response, important for fast vehicle response, and 3) has no position overshoot, which increased reliability in applications such as landmine detection.

Further investigations into the equilibrated system could be done in the future. Implementing a different type of controller, such as an LQR controller (Linear Quadratic Regulator), instead of a PID controller used in this research might give better results. In addition, using the results presented in this thesis and the work by Shin and Streit [10], equilibrators could be implemented on a serial manipulator to verify if pick-and-place motions are more accurate and faster as this research suggests. Also, research could be done to compare optimized dimensions found from simulations to an actual equilibrated system. Finally, research into the comparison of power requirements for each system could be analyzed in the future.

## BIBLIOGRAPHY

1. Franklin, G. F, Powell, J. D. and Workman, M. Digital Control of Dynamic Systems. Reading, Mass: Addison Wesley Longman, Inc. Third Edition, 1998.
2. Friedland, B. Control System Design: An Introduction to State-Space Methods. New York: McGraw-Hill, Inc. 1986.
3. Hain, K. "Spring Mechanisms- Point Balancing." and "Spring Mechanisms: Continuous Balancing." *Spring Design and Application*.. Chironis, N., ed., McGraw-Hill, New York, 1961, pp. 268-275.
4. Inman, D. J. *Engineering Vibration*. New Jersey: Prentice Hall, Second Edition, 2001.
5. Meriam, J.L. and Kraige, L.G. Dynamics. New York: John Wiley & Sons, Inc. Vol. 2, Third Edition, 1992.
6. Mitchell, Larry. Class Notes: Signal Processing for Experimental Analysis. Virginia Polytechnic Institute and State University, Mechanical Engineering Department. ME 5714, Fall 2000.
7. Nathan, R. M, "A Constant Force Generation Mechanism," *ASME Journal of Mechanisms, Transmissions, and Automation in Design*, Dec 1985, Vol. 107, No. 4, pp. 508-512.
8. Pons.J.L., Ceres, R, and Jimenez, A.R. "Quasi-Exact Linear Spring Countergravity System for Robotic Manipulators." *Mechanism and Machine Theory*, Feb 1998, Vol. 33, pp 59-70.
9. Shetty, Devdas and Kolk, Richard. Mechatronics System Design. Boston, MA: PWS Publishing Company, pg. 212-213, 1997.
10. Shin, E., and Streit, D. A., "An Energy Efficient Quadruped with Two-State Equilibrator." *ASME Journal of Mechanical Design*, March 1993, Vol. 115, pp 156-163.
11. Shin, E., and Streit, D. A., "Spring Equilibrator Theory for Static Balancing of Planar Pantograph Linkages." *Mechanical Machine Theory*, April 1991, Vol. 26, No. 7. pp 645-657.
12. Streit, D. A, Chung, H, and Gilmore, B.J. "Perfect Equilibrators for Rigid Body Spatial Rotations About a Hooke's Joint," *ASME Journal of Mechanical Design*, Dec. 1991, Vol. 113, pp. 500-507.
13. Streit, D. A, and Gilmore, B.J. "Perfect Spring Equilibrators for Rotatable Bodies," *ASME Journal of Mechanisms, Transmissions, and Automation in Design*, Dec. 1989, Vol. 111, No. 4, pp. 451-458.
14. Streit, D. A., and Shin, E., "Equilibrators for Planar Linkages." *ASME Journal of Mechanical Design*, Sept. 1993, Vol. 115, pp. 604-611.

15. VT Mechatronics Home Page. *Procedure for Identifying Permanent Magnet DC Motors*.  
<http://www.mechatronics.me.vt.edu/book/Section3/motormodelling.html>, pg. 1-16.
16. Walsh, G. J., Streit, D. A., and Gilmore, B. J., "Spatial Spring Equilibrator Theory."  
*Mechanism and Machine Theory*, 1991, Vol. 26, No. 2, pp 155-170.
17. Walsh, G. J., Streit, D. A., and Gilmore, B. J., "Perfect Spring Equilibrators for Spatial Two Degree-of-Freedom Rotatable Bodies." *ASME, Design Engineering Division*, 1988, pp 497-503.

# Appendix A: Mathematica Code

## Equilibrated System- Dynamic EOM

■ This code includes the motor and equilibrator EOMs. This is used in the DYNAMIC PID control of the closed loop response of the equilibrated system.

```
Off[General::spell1];
```

### Equilibrator Position Solutions

```
Rules = {B -> .23495, C -> .263525, r -> .00635, J ->  $\frac{\text{mechtime} * Kb * Kt}{Ra}$ , Kt -> Kb, Kb -> 5.456 *  $\frac{1}{(1000+2+2\pi)}$ , K -> 77.3235, R -> .33655,
M -> 1.34, m -> .2268, g -> 9.81, xi -> 0, damp -> .19, mechtime -> .0013333, Ra -> 2.24};

lrule = {l[t] ->  $\sqrt{(B^2 + C^2 - 2 B C \text{Sin}[\theta[t]] - r^2)}$ };
 $\theta$ rule = { $\theta$ [t] ->  $\pi / 2 - \text{ArcSin}[r / C]$ };
 $\varphi$ rule = { $\varphi$ [t] ->  $\{2 \pi + 2 \text{ArcTan}[(B \text{Cos}[\theta[t]] - l[t]), (r - \sqrt{r^2 - B^2 * (\text{Cos}[\theta[t]]^2 + (l[t])^2})]\}$ };
l0 = {-B +  $\sqrt{C^2 - r^2}$ };
 $\varphi$ 0 =  $\varphi$ [t] /.  $\varphi$ rule /.  $\theta$ rule /. {l[t] -> l0} // Simplify;
```

■ Position loop equation to find  $\varphi$  (using tangent of half angle)  
(How solved for the correct closure to use in  $\varphi$ rule is below)

```
PositionEq = B ei $\varphi$ [t] + l[t] ei $\theta$ [t] + r i ei $\varphi$ [t] - C i;
```

```
ExpToTrig[PositionEq]
```

```
-i C + B Cos[ $\theta$ [t]] + i r Cos[ $\varphi$ [t]] + Cos[ $\varphi$ [t]] l[t] + i B Sin[ $\theta$ [t]] - r Sin[ $\varphi$ [t]] + i l[t] Sin[ $\varphi$ [t]]
```

```
PositionEqReal = l[t] Cos[ $\varphi$ [t]] - r Sin[ $\varphi$ [t]] + B Cos[ $\theta$ [t]];
```

```
PositionEqImag = l[t] Sin[ $\varphi$ [t]] + r Cos[ $\varphi$ [t]] - (C - B Sin[ $\theta$ [t]]);
```

```
urule = {u[t] -> Tan[ $\varphi$ [t] / 2]};
```

```
cos $\varphi$ rule = {Cos[ $\varphi$ [t]] ->  $\frac{1 - u[t]^2}{1 + u[t]^2}$ };
```

```
sin $\varphi$ rule = {Sin[ $\varphi$ [t]] ->  $\frac{2 u[t]}{1 + u[t]^2}$ };
```

```
Simplify[Solve[(PositionEqReal /. cos $\varphi$ rule /. sin $\varphi$ rule) == 0, u[t]]]
```

```
Simplify[Solve[(PositionEqImag /. cos $\varphi$ rule /. sin $\varphi$ rule) == 0, u[t]]]
```

```
{u[t] ->  $\frac{r - \sqrt{r^2 - B^2 \text{Cos}[\theta[t]]^2 + l[t]^2}}{B \text{Cos}[\theta[t]] - l[t]}$ }, {u[t] ->  $\frac{r + \sqrt{r^2 - B^2 \text{Cos}[\theta[t]]^2 + l[t]^2}}{B \text{Cos}[\theta[t]] - l[t]}$ }}
```

```
{u[t] ->  $\frac{l[t] - \sqrt{-C^2 + r^2 + l[t]^2 + 2 B C \text{Sin}[\theta[t]] - B^2 \text{Sin}[\theta[t]]^2}}{C + r - B \text{Sin}[\theta[t]}}$ }, {u[t] ->  $\frac{l[t] + \sqrt{-C^2 + r^2 + l[t]^2 + 2 B C \text{Sin}[\theta[t]] - B^2 \text{Sin}[\theta[t]]^2}}{C + r - B \text{Sin}[\theta[t]}}$ }}
```

Then I hand calculated  $\varphi$  using some representative values to find the correct u

```
Chop[Solve[(PositionEqReal /. cos $\varphi$ rule /. sin $\varphi$ rule) == 0, u[t]] /. l[t] -> l0 /.  $\theta$ rule /. Rules]
```

```
{u[t] -> 0.976187}, {u[t] -> -1.5323}}
```

```
Chop[Solve[(PositionEqImag /. cos $\varphi$ rule /. sin $\varphi$ rule) == 0, u[t]] /. l[t] -> l0 /.  $\theta$ rule /. Rules]
```

```
{u[t] -> 0.652613}, {u[t] -> 0.976187}}
```

```
den = B Cos[ $\theta$ [t]] - l[t] /. l[t] -> l0 /.  $\theta$ rule /. Rules;
```

```
num = r -  $\sqrt{r^2 - B^2 \text{Cos}[\theta[t]]^2 + l[t]^2}$  /. l[t] -> l0 /.  $\theta$ rule /. Rules;
```

```
ArcTan[den, num] * (180 /  $\pi$ ) * 2
```

```
-271.381
```

```
( $\varphi$ 0 /. Rules) * (180 /  $\pi$ )
```

```
88.6192
```

```
( $\theta$ [t] /.  $\theta$ rule /. Rules) * (180 /  $\pi$ )
```

```
88.6192
```

---

$\theta$  and  $\varphi$  are same value at ( $\theta$ )

■ Rules to define  $\Delta x$  for Dynamics (Lagrange Potential Energy)

```
Alrule = {Al[t] -> (l[t])};
Asrule = {As[t] -> (r (-phi[t] + phi))};
Axrule = {Ax[t] -> (xi + As[t] + Al[t]) /. Alrule /. Asrule /. phiRule /. lrule};
```

■ Rules to transform from the Complex Notation to Real Notation

```
complexRule1 = {Re[s_] -> s, Im[s_] -> 0};
complexRule2 = {Re[sj_] -> sj, Im[sj_] -> 0};
ComplexToRealCoord[f_] := {Re[f // ComplexExpand],
Im[f // ComplexExpand]} /. complexRule1 /. complexRule2;
```

■ Input Coordinate System and Position Vectors

```
i = {1, 0}; j = {0, 1};
LMPComplex[t] = R Exp[I theta[t]];
RodComplex[t] = R/2 Exp[I theta[t]];

LMP[t] = ComplexToRealCoord[LMPComplex[t]];
Rod[t] = ComplexToRealCoord[RodComplex[t]];
```

Equilibrator Dynamics ( $d\phi=d\varphi$ )

■ System Damping

```
JointDamping = 1/2 damp (D[theta[t], t])^2;
```

■ Input Kinetic Potential Energy and Rayleigh Dissipation Function

```
Ttheta = 1/2 (MD[LMP[t], t].D[LMP[t], t] + 1/3 m R^2 theta'[t]^2 + J (theta'[t] Gr)^2);
Vtheta = g (M (LMP[t].j) + m (Rod[t].j));
Vx = 1/2 k (Ax[t] /. Axrule)^2;

Ray = JointDamping;
T = Simplify[(Ttheta)];
V = (Vtheta + Vx);
```

■ The Euler-Lagrange equations

```
lagrangian = T - V;
EOM[coord_] := D[D[lagrangian, D[coord, t]], t] - D[lagrangian, coord] + D[Ray, D[coord, t]];
```

■ Equations of Motion

```
Qtheta = Kt Current[t];
eqi = La Current'[t] + Ra Current[t] + Kb theta'[t] Gr - Va;
```

Result of Lagrange

```
eqtheta = EOM[theta[t]] - Qtheta;
```

■ Nonlinear Solutions

```
Solutions = Solve[{eqtheta == 0, eqi == 0}, {theta'[t], Current'[t]}]
{{Current'[t] -> - (Va + Ra Current[t] + Gr Kb theta'[t]) / La,
theta'[t] -> - 1 / (3 Gr^2 J + (m + 3 M) R^2) (3 (g (1/2 m R Cos[theta[t]] + M R Cos[theta[t]]) - Kt Current[t] + k (xi + r (-2 pi + 2
```

$$\left( \pi + \text{ArcTan}\left[ B + \frac{B r}{C} - \sqrt{C^2 - r^2}, r - \sqrt{B^2 + C^2 - \frac{B^2 r^2}{C^2} - 2B \sqrt{C^2 - r^2}} \right] - 2 \text{ArcTan}\left[ B \cos[\theta[t]] - \sqrt{B^2 + C^2 - r^2 - 2BC \sin[\theta[t]]}, \right. \right. \\ \left. \left. r - \sqrt{B^2 + C^2 - B^2 \cos[\theta[t]]^2 - 2BC \sin[\theta[t]]} \right] + \sqrt{B^2 + C^2 - r^2 - 2BC \sin[\theta[t]]} \right) \\ \left( \frac{BC \cos[\theta[t]]}{\sqrt{B^2 + C^2 - r^2 - 2BC \sin[\theta[t]]}} - \left( 2 r \left( (-2BC \cos[\theta[t]] + 2B^2 \cos[\theta[t]] \sin[\theta[t]]) (B \cos[\theta[t]] - \sqrt{B^2 + C^2 - r^2 - 2BC \sin[\theta[t]]}) - \right. \right. \right. \\ \left. \left. \left. \sqrt{B^2 + C^2 - r^2 - 2BC \sin[\theta[t]]} \right) \right) / \left( 2 \sqrt{B^2 + C^2 - B^2 \cos[\theta[t]]^2 - 2BC \sin[\theta[t]]} \right) - \right. \\ \left. \left( -B \sin[\theta[t]] + \frac{BC \cos[\theta[t]]}{\sqrt{B^2 + C^2 - r^2 - 2BC \sin[\theta[t]]}} \right) \left( r - \sqrt{B^2 + C^2 - B^2 \cos[\theta[t]]^2 - 2BC \sin[\theta[t]]} \right) \right) \right) / \\ \left( \left( B \cos[\theta[t]] - \sqrt{B^2 + C^2 - r^2 - 2BC \sin[\theta[t]]} \right)^2 + \left( r - \sqrt{B^2 + C^2 - B^2 \cos[\theta[t]]^2 - 2BC \sin[\theta[t]]} \right)^2 \right) + \text{damp } \theta' [t] \Big) \Big) \Big\}$$

**RenameRule = {θ[t] → Theta, θ'[t] → ThetaDot, Current[t] → Current};**

**ThetaDotDot = InputForm[θ''[t] /. Solutions /. RenameRule];**

■ Taylor Series Expansion to Linearize about θ=0 (Used first two terms of expansion)

**Term1 = θ'[t] /. Solutions /. RenameRule /. {Theta → 0};**

**Term2 = θ''[t] /. Solutions /. RenameRule /. {Theta → 0};**

**LinearEquationofMotion = Term1 + Term2 + Theta**

$$\left\{ -\frac{1}{3 Gr^2 J + (m + 3M) R^2} \left( 3 \text{Theta} \left[ k \left( -\frac{BC}{\sqrt{B^2 + C^2 - r^2}} - \frac{2 r \left( -\frac{B r (\sqrt{C^2 + r^2})}{\sqrt{B^2 + C^2 - r^2}} + \frac{B r (B - \sqrt{B^2 + C^2 - r^2})}{\sqrt{C^2}} \right)}{(-\sqrt{C^2} + r)^2 + (B - \sqrt{B^2 + C^2 - r^2})^2} \right) + \right. \right. \\ \left. \left. k \left( -\frac{B^2 C^2}{(B^2 + C^2 - r^2)^{3/2}} + \frac{2 r \left( -\frac{B r (\sqrt{C^2 + r^2})}{\sqrt{B^2 + C^2 - r^2}} + \frac{B r (B - \sqrt{B^2 + C^2 - r^2})}{\sqrt{C^2}} \right) \left( \frac{2 B r (\sqrt{C^2 + r^2})}{\sqrt{C^2}} + \frac{2 B r (B - \sqrt{B^2 + C^2 - r^2})}{\sqrt{B^2 + C^2 - r^2}} \right)}{((- \sqrt{C^2} + r)^2 + (B - \sqrt{B^2 + C^2 - r^2})^2)^2} + \frac{2 r (-\sqrt{C^2} + r) \left( -B + \frac{B^2 C^2}{(B^2 + C^2 - r^2)^{3/2}} \right)}{(-\sqrt{C^2} + r)^2 + (B - \sqrt{B^2 + C^2 - r^2})^2} \right) \right. \right. \\ \left. \left. \left( \sqrt{B^2 + C^2 - r^2} + x_1 + r \left( -2 \pi + 2 \left( \pi + \text{ArcTan}\left[ B + \frac{B r}{C} - \sqrt{C^2 - r^2}, r - \sqrt{B^2 + C^2 - \frac{B^2 r^2}{C^2} - 2B \sqrt{C^2 - r^2}} \right] - \right. \right. \right. \right. \right. \\ \left. \left. \left. 2 \text{ArcTan}\left[ B - \sqrt{B^2 + C^2 - r^2}, -\sqrt{C^2} + r \right] \right) \right) \right) \right) - \frac{1}{3 Gr^2 J + (m + 3M) R^2} \\ \left. \left( \left( -\text{Current} K t + g \left( \frac{m R}{2} + M R \right) + \text{damp } \text{ThetaDot} + k \left( -\frac{BC}{\sqrt{B^2 + C^2 - r^2}} - \frac{2 r \left( -\frac{B r (\sqrt{C^2 + r^2})}{\sqrt{B^2 + C^2 - r^2}} + \frac{B r (B - \sqrt{B^2 + C^2 - r^2})}{\sqrt{C^2}} \right)}{(-\sqrt{C^2} + r)^2 + (B - \sqrt{B^2 + C^2 - r^2})^2} \right) \left( \sqrt{B^2 + C^2 - r^2} + \right. \right. \right. \right. \\ \left. \left. \left. x_1 + r \left( -2 \pi + 2 \left( \pi + \text{ArcTan}\left[ B + \frac{B r}{C} - \sqrt{C^2 - r^2}, r - \sqrt{B^2 + C^2 - \frac{B^2 r^2}{C^2} - 2B \sqrt{C^2 - r^2}} \right] - 2 \text{ArcTan}\left[ B - \sqrt{B^2 + C^2 - r^2}, -\sqrt{C^2} + r \right] \right) \right) \right) \right) \right) \right) \Big\}$$

**InputForm[LinearEquationofMotion];**

**LinearEquationofMotion1 = Collect[LinearEquationofMotion, {ThetaDot, Theta, Current}];**

$$\left\{ \frac{3 \text{Current} K t}{3 Gr^2 J + (m + 3M) R^2} - \frac{3 g \left( \frac{m R}{2} + M R \right)}{3 Gr^2 J + (m + 3M) R^2} - \frac{3 \text{damp } \text{ThetaDot}}{3 Gr^2 J + (m + 3M) R^2} - \right.$$

$$\frac{1}{3 Gr^2 J + (m + 3 M) R^2} \left( 3 \text{Theta} \left( k \left( \frac{B C}{\sqrt{B^2 + C^2 - r^2}} - \frac{2 r \left( \frac{B c \left( \sqrt{c^2 + r} \right) + B c \left( B - \sqrt{B^2 + C^2 - r^2} \right)}{\sqrt{B^2 + C^2 - r^2}} + \frac{B c \left( B - \sqrt{B^2 + C^2 - r^2} \right)}{\sqrt{c^2}} \right)}{(-\sqrt{C^2} + r)^2 + (B - \sqrt{B^2 + C^2 - r^2})^2} \right) + k \left( \frac{B^2 C^2}{(B^2 + C^2 - r^2)^{3/2}} + \right. \right. \\ \left. \left. \frac{2 r \left( \frac{B c \left( \sqrt{c^2 + r} \right) + B c \left( B - \sqrt{B^2 + C^2 - r^2} \right)}{\sqrt{B^2 + C^2 - r^2}} + \frac{B c \left( B - \sqrt{B^2 + C^2 - r^2} \right)}{\sqrt{c^2}} \right) \left( \frac{r B c \left( \sqrt{c^2 + r} \right) + r B c \left( B - \sqrt{B^2 + C^2 - r^2} \right)}{\sqrt{B^2 + C^2 - r^2}} + \frac{r B c \left( B - \sqrt{B^2 + C^2 - r^2} \right)}{\sqrt{B^2 + C^2 - r^2}} \right)}{((- \sqrt{C^2} + r)^2 + (B - \sqrt{B^2 + C^2 - r^2})^2)} + \frac{2 r (-\sqrt{C^2} + r) \left( -B + \frac{B^2 C^2}{(B^2 + C^2 - r^2)^{3/2}} \right)}{(-\sqrt{C^2} + r)^2 + (B - \sqrt{B^2 + C^2 - r^2})^2} \right) \left( \sqrt{B^2 + C^2 - r^2} + \right. \\ \left. \left. x_1 + r \left( -2 \pi + 2 \left( \pi + \text{ArcTan} \left[ B + \frac{B r}{C} - \sqrt{C^2 - r^2}, r - \sqrt{B^2 + C^2 - \frac{B^2 r^2}{C^2} - 2 B \sqrt{C^2 - r^2}} \right] \right) - 2 \text{ArcTan} \left[ B - \sqrt{B^2 + C^2 - r^2}, -\sqrt{C^2} + r \right] \right) \right) \right) \\ \frac{1}{3 Gr^2 J + (m + 3 M) R^2} \left( 3 k \left( -\frac{B C}{\sqrt{B^2 + C^2 - r^2}} - \frac{2 r \left( \frac{B c \left( \sqrt{c^2 + r} \right) + B c \left( B - \sqrt{B^2 + C^2 - r^2} \right)}{\sqrt{B^2 + C^2 - r^2}} + \frac{B c \left( B - \sqrt{B^2 + C^2 - r^2} \right)}{\sqrt{c^2}} \right)}{(-\sqrt{C^2} + r)^2 + (B - \sqrt{B^2 + C^2 - r^2})^2} \right) \left( \sqrt{B^2 + C^2 - r^2} + x_1 + \right. \\ \left. \left. r \left( -2 \pi + 2 \left( \pi + \text{ArcTan} \left[ B + \frac{B r}{C} - \sqrt{C^2 - r^2}, r - \sqrt{B^2 + C^2 - \frac{B^2 r^2}{C^2} - 2 B \sqrt{C^2 - r^2}} \right] \right) - 2 \text{ArcTan} \left[ B - \sqrt{B^2 + C^2 - r^2}, -\sqrt{C^2} + r \right] \right) \right) \right) \right)$$

**U = Coefficient [LinearEquationOfMotion, Theta];**

**T = Coefficient [LinearEquationOfMotion, ThetaDot]**

**InputForm [T];**

$$\left\{ -\frac{3 \text{damp}}{3 Gr^2 J + (m + 3 M) R^2} \right\}$$

**S = Coefficient [LinearEquationOfMotion, Current]**

**InputForm [S];**

$$\left\{ \frac{3 K r}{3 Gr^2 J + (m + 3 M) R^2} \right\}$$

**ThetaDotDotConstant = Simplify [LinearEquationOfMotion1 - U Theta - T ThetaDot - S Current]**

**InputForm [ThetaDotDotConstant];**

$$\left\{ \frac{1}{3 Gr^2 J + (m + 3 M) R^2} \left( 3 \left( -\frac{1}{2} g (m + 2 M) R - \right. \right. \right. \\ \left. \left. \left( B C k \left( \sqrt{C^2} - r \right) \left( B^2 + C^2 - r^2 - B \sqrt{B^2 + C^2 - r^2} \right) \left( \sqrt{B^2 + C^2 - r^2} + x_1 + 2 r \text{ArcTan} \left[ B + \frac{B r}{C} - \sqrt{C^2 - r^2}, r - \sqrt{B^2 + C^2 - \frac{B^2 r^2}{C^2} - 2 B \sqrt{C^2 - r^2}} \right] - \right. \right. \right. \\ \left. \left. \left. 2 r \text{ArcTan} \left[ B - \sqrt{B^2 + C^2 - r^2}, -\sqrt{C^2} + r \right] \right) \right) / \left( \sqrt{C^2} \sqrt{B^2 + C^2 - r^2} \left( -B^2 - C^2 + \sqrt{C^2} r + B \sqrt{B^2 + C^2 - r^2} \right) \right) \right) \right\}$$

**Usimp = Simplify [Coefficient [LinearEquationOfMotion, Theta]]**

**InputForm [Usimp];**

$$\left\{ -\frac{1}{3 Gr^2 J + (m + 3 M) R^2} \right. \\ \left. \left( 3 B k \left( \frac{B C^2 \left( -1 + \frac{r \left( -B^2 + r \left( \sqrt{c^2 + r} \right) + B \sqrt{B^2 + C^2 - r^2} \right)}{\sqrt{c^2} \left( -B^2 - C^2 + \sqrt{C^2} r + B \sqrt{B^2 + C^2 - r^2} \right)} \right)}{B^2 + C^2 - r^2} \right) + \left( -2 B^3 \left( C^2 - \sqrt{C^2} r \right) + 2 B^2 \left( C^2 - \sqrt{C^2} r \right) \sqrt{B^2 + C^2 - r^2} - B \left( C^4 - 3 C^2 r^2 + 2 \sqrt{C^2} r^3 \right) + \right. \right. \\ \left. \left. r \sqrt{B^2 + C^2 - r^2} \left( -2 C^2 r + \sqrt{C^2} \left( C^2 + r^2 \right) \right) \left( \sqrt{B^2 + C^2 - r^2} + x_1 + 2 r \text{ArcTan} \left[ B + \frac{B r}{C} - \sqrt{C^2 - r^2}, r - \sqrt{B^2 + C^2 - \frac{B^2 r^2}{C^2} - 2 B \sqrt{C^2 - r^2}} \right] - \right. \right. \right. \\ \left. \left. \left. 2 r \text{ArcTan} \left[ B - \sqrt{B^2 + C^2 - r^2}, -\sqrt{C^2} + r \right] \right) \right) / \left( \sqrt{B^2 + C^2 - r^2} \left( B^2 + C^2 - \sqrt{C^2} r - B \sqrt{B^2 + C^2 - r^2} \right) \right) \right) \right\}$$

## **Vita**

Angela S. Carr was born, along with Jillian L. Carr, on December 19, 1975 in Rockford, Illinois. After only six months, her mother and father, Barbara and Charles, moved three young children and a household to Appomattox, Virginia. Angela spent her childhood there, and later attended Appomattox County High School and Central Virginia Governor's School. She developed her hobbies of reading, gardening, and running during this time. It was also during this time that Angela decided to be an engineer. Following that dream, lead her to her undergraduate studies at Virginia Polytechnic Institute and State University, her Dad's alma mater. After completion, Angela traveled Europe for a while, and then started her graduate work at VPI & SU. She will be beginning her post-graduate career with Ingersoll-Rand. Her first job assignment is with the Torrington Division working for the Georgia Technology Excellence Center in Atlanta GA.